REPORT NO. 2
INTERIM REPORT
TESTING METHODOLOGIES FOR FIBER
OPTIC TRANSMISSION SYSTEMS

Prepared by
Bell-Northern Research Ltd.
Ottawa, Ontario

SEPTEMBER 1981

REPORT NO. 2
INTERIM REPORT
TESTING METHODOLOGIES FOR FIBER OPTIC TRANSMISSION SYSTEMS

FOR: Department of Communications
Communications Research Center
P.O. Box 11490, Station H,
Ottawa, Ontario K2H 8S2
Attn: Shirley Bay

DSS File Reference: 13ST. 36061-0-3309
DSS Contract Serial: 1ST80-00116
BNR Reference: P372/TR6734

Prepared By: Bell-Northern Research Ltd.
P.O. Box 3511, Station C,
Ottawa, Ontario
K1Y 4H7

Government of Canada
Department of Communications

DOC CONTRACTOR REPORT

DOC-CR-CS-81-0025

DEPARTMENT OF COMMUNICATIONS - OTTAWA - CANADA
COMMUNICATION SYSTEMS RESEARCH AND DEVELOPMENT

TITLE: INTERIM REPORT - TESTING METHODOLOGIES FOR FIBER OPTIC TRANSMISSION SYSTEMS

AUTHORS(S): N/A

ISSUED BY CONTRACTOR AS REPORT NO: N/A

CONTRACTOR: BELL-NORTHERN RESEARCH LTD.

DEPARTMENT OF SUPPLY AND SERVICES CONTRACT NO: 1ST80-00116

DOC SCIENTIFIC AUTHORITY: METIN B. AKGUN

CLASSIFICATION: UNCLASSIFIED

This report presents the views of the author(s). Publication of this report does not constitute DOC approval of the report's findings or conclusions. This report is available outside the Department by special arrangement.

DATE: SEPTEMBER 1981

SUMMARY

This report describes the current status of modelling activities aimed at establishing test methods for fiber optic links and components.

The fiber has been characterized by three different approaches. Its impulse response has been measured experimentally as well as computed from its index profile and from differential mode characteristics. The three impulse responses are compared.

Launching conditions have been simulated to represent both the mode volume and the power profile (near-field pattern) of a source. A relationship between the modal power distribution and the near-field pattern is being sought. The complexities of this research are discussed.

The fibre joint has been modelled partially. Matching conditions have been established between incoming and outgoing modes.

Future activities are discussed.

TABLE OF CONTENTS

LIST OF FIGURES

page

LIST OF TABLES

Page

1. INTRODUCTION

1.1 Objective of the Contract

The objective of this contract is the definition of testing methods for fiber optic transmission systems. These test methods should result in:

- better characterization of fiber components,
- better and more cost-effective system design,
- improved maintenance, and
- more meaningful standards for fiber components.

To these ends, a model is being developed with both a theoretical and an experimental basis. The model represents the fundamental behaviour of fiber systems. The fiber components are represented by their modal characteristics: differential mode delay and attenuation, mode coupling, and modal excitation.

During the remainder of the contract, various testing methods will be simulated using the model to assess their suitability against the stated objectives.

1.2 Objective of the Report

The objective of this report is to present the status of the modelling activities and discuss ongoing activities in order to fulfill the objective of the contract.

1.3 Outline of the Report

Section 2 presents the conclusions of the activities to-date and comments on the forthcoming activities.

Section 3 discusses the theoretical aspects of the modelling of the fiber, joint and source.

Section 4 describes the experimental facilities used to acquire the data.

Section 5 presents the results of the theoretical simulation and of the experiments. The theoretical and experimental results are compared where applicable.

Section 6 discusses further work.

This report fulfills milestone 2 of the contract as per the work proposal.

2. CONCLUSIONS

2.1 Status

To provide data input for the theoretical modelling, an extensive measurement facility is in place. Certain aspects have been custom-designed to meet the needs of this study. The capability includes measurement of the fiber refractive index profile, attenuation, and time-domain dispersion Fourier-transformable to the frequency domain. Moreover, selective mode excitation has been used to probe differential attenuation and differential delay. The measurement facility can also accomodate selective mode detection, and concatenations of a number of fiber sections as may be required in subsequent modelling activity.

The impulse response of a fiber has been measured directly in the time domain and predicted theoretically by two independent methods. The first method uses the experimentally measured profile and the Wentzel, Kramers and Brillouin (WKB) model. The second method uses the experimentally measured differential mode attenuation and delay. The WKB approach tends to overestimate the width of the impulse response while the differential mode approach tends to underestimate it. Both theoretical approaches predict multiple peaks in the response while the measured impulse response is single-peaked.

In both cases, obtaining the impulse response requires a knowledge of the launching conditions, i.e. either the modal power distribution or else the radiation pattern of the source. Simulations have shown the dependency of pulse shape and pulse width on the excitation conditions. In particular it was shown that the pulse broadening is not uniquely determined by the mode volume of the launch beam. Peaks in the response have also been shown to depend on the launching conditions.

The inclusion of leaky modes hardly changes the impulse response as only a few modes have an attenuation less than 10dB/km.

The need to know the excitation conditions at the fiber input prompted an investigation of the relationship between the near-field pattern (NFP) at the fiber end face and the modal power distribution (MPD) in the same plane.

Two approaches were taken: a geometrical optic approach and a field theory approach. In the geometrical optic case a linear expression was found to relate the NFP and radiance. Under uniform radiance, the computed NFP reveals, as expected, the main features of the index profile. However, the inverse linear transformation results in non-uniform and negative-valued radiance when the NFP is assumed equal to the index profile. Furthermore, the linear transformation needs further research to substantiate its physical interpretation.

The field theory approach expresses the NFP as a linear combination of the power in all modes. The power is determined via the WKB model. In this case, the inverse linear transformation also led to a negative valued MDP when the NFP was assumed equal to the index profile. This may be caused by the inaccuracy of the WKB method in the vicinity of the caustics.

The joint model indicates qualitatively how the power is transferred from one mode to another for a given relative offset. At a relative offset of

20%, with identical transmitting and receiving fibers the coupling is predominantly to modes having a propagation constant β within a window about the β of the exciting mode. The width of this window increases as β decreases.

2.2 Future Activities

Forthcoming activities will focus on

- characterizing further the impulse response of sample fibers,

- improving the modelling of the excitation conditions that correspond to the input power of the time domain response measurement, and

- resolving the problem of determining the modal power distribution from near-field pattern measurements. A successful solution may lead to a relatively simple method to measure differential mode delay and attenuation.

Fiber measurements will be pursued to include the characterization of crosscoupling and skew rays.

The theoretical model of the joint will be pursued to incorporate the quantitative power transfer that takes place at all points of core overlap where mode matching conditions have been found. The joint will also be characterized experimentally.

The analysis and evaluation of promising launch conditioning devices for test methods will commence.

On the basis of both the theoretical and experimental studies, recommendations will be made on test methods suitable for the measurement of attenuation and bandwidth of fiber links.

3. THEORETICAL ASPECTS OF THE MODEL

The first phase of the work consists of modelling the components of a fibre system, i.e. the fiber, the source and the joints. These components are modelled both theoretically and experimentally. The models will be used in the second phase of the work to simulate and assess various testing methods.

As per the Orientation Report issued in March 1981 for the first milestone of this contract, a WKB approach is chosen to model the fiber in a quasi-ray theory fashion and to characterize its modal behaviour. The source model is also developed on the basis of geometrical optics in a first approach and on the basis of WKB field theory in a second approach. The joint model incorporates a WKB characterization of the modes into a ray optics representation.

3.1 Fiber

3.1.1 Rays and Modes

The theoretical basis for the fiber model is a blend of geometrical ray optics and Maxwellian wave optics. The two can be related by a WKB theory suitable for multimode fibers. (The small optical dimensions of monomode fibers necessitate wave optics there). A general outline of ray and wave optics results is given here; much is now standard in older papers and recent texts, but some is not well known or else very new. Proofs are omitted.

Ray optics for a dielectric begins with the general equation

$$\frac{d}{dS}\left[n(\bar{R})\,\overline{\frac{dR}{dS}}\,\right] = \text{grad } n(\bar{R}) \quad . \tag{3.1.1}$$

Here $\bar{R}$ is the position vector of any point along the ray (referenced to an arbitrary fixed origin) at which the refractive index has the known value $n(\bar{R})$. S is the ray path length (referenced to an arbitrary fixed point on the ray), and $d\bar{R}/dS$ is a unit vector tangent to the ray path. As in Figure 3.1, a cylindrical (r,ψ,z) coordinate system is appropriate for fibers; the refractive index $n(r)$ does not vary axially with z or azimuthally with ψ, but depends only on the radial distance r.

It is found that the ray tangent is described by a wavevector of magnitude $kn(r)$, where $k = 2\pi/\lambda$ in vacuum, and its (r,ϕ,z) components are

$$q(r) = kn(r)\sin\Theta(r)\sin\phi(r) = \sqrt{k^2n^2(r) - \nu^2/r^2 - \beta^2} \tag{3.1.2}$$

$$\nu/r = kn(r)\sin\Theta(r)\cos\phi(r) = \sqrt{k^2n^2(r) - \beta^2}\cos\phi(r)$$

$$\beta = kn(r)\cos\Theta(r)$$

In Figure 3.1, $\Theta(r)$ is the angle between the ray at r and the z-axis while $\phi(r)$ is the angle between the ψ-component of the ray and the r-axis; sin ϕ and cos ϕ are interchangeable. Two symbols have been introduced to describe quantities that are found to be conserved along a ray: β the axial or propagation wavenumber (analogous to ray 'energy') and ν (not ν/r) the azimuthal number (analogous to ray "angular momentum'). Hence the ray may be specified by the variable (r,Θ,ϕ) along its path, or else by its 'constants' (β,ν) within the guide.

At this point the relationship of the above to wave optics is examined. Beginning with Maxwell's equations and the material constitutive relations, a wave equation can be derived. For a guide, the electromagnetic fields are harmonic in time (with an angular frequency ω=ck) and in axial distance (with an axial spatial frequency β); moreover the variation of the refractive index is on the order of 1%. All this leads to an approximate scalar transverse waveguide equation which for crosssectional circular symmetry becomes

$$\frac{d^2E}{dr^2} + q^2(r)E(r) = 0 \qquad (3.1.3.a)$$

with the fields

$$E(r)r^{-\frac{1}{2}}e^{i(\beta z-\omega t\pm\nu\phi)} \qquad (3.1.3.b)$$

The β,ν,q notation here is the same as for the ray notation, as can be shown via the WKB method (which has several formulations). This method has the advantage that the fields E (and the associated optical power) can be determined for each ray; they are of the form

$$E_\mu(r) = (rq(r))^{-\frac{1}{2}}A_\mu \exp(\pm i\int^r q(r)dr+X_\mu) \qquad (3.1.4)$$

where A_μ and X_μ are complex constants.

Wherever q(r) is real, the fields are oscillatory in the radial coordinate r, possessing μ nodes such that

$$(\mu + \tfrac{1}{2})\pi = \int_{R_1}^{R_2} q(r)\, dr, \quad \mu=0,1,2,... \qquad (3.1.5)$$

Here R_1 and R_2 are respectively the inner and outer 'caustics' $q(R_1)=q(R_2) = 0$ between which q is real. For radial positions $r<R_1$ and $r>R_2$, q is imaginary and the fields are exponentially evanescent. Equation (3.1.5) is a 'characteristic' equation that determines the propagation constant β as a function of the numbers μ and ν. It is a standing wave phase condition in the radial direction; when similarly applied to the azimuthal wavenumber ν/r, around any circumference $2\pi r$, ν must be an integer. Hence a ray may be specified in terms of the constants (β, ν), with β having discrete allowed values via Equation (3.1.5) and ν an integer, or else in terms of the integer mode number pair (μ, ν).

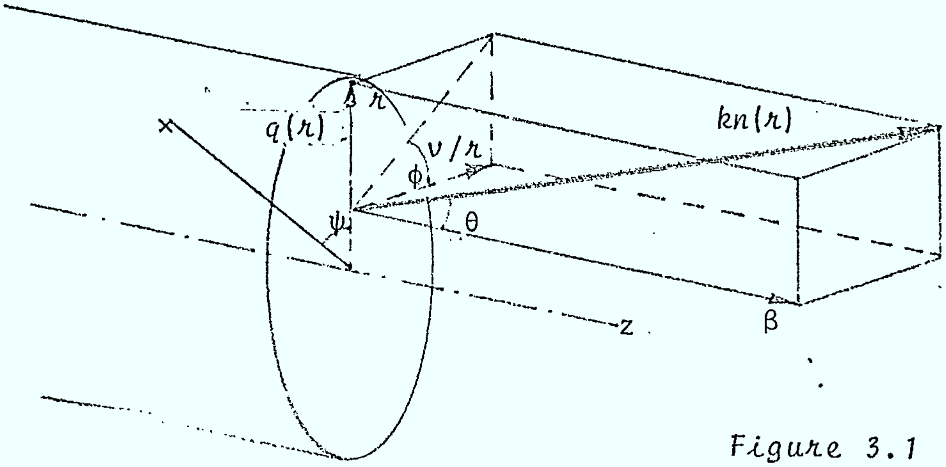

Figure 3.1 Propagation Vector and its Components in cylindrical Coordinates

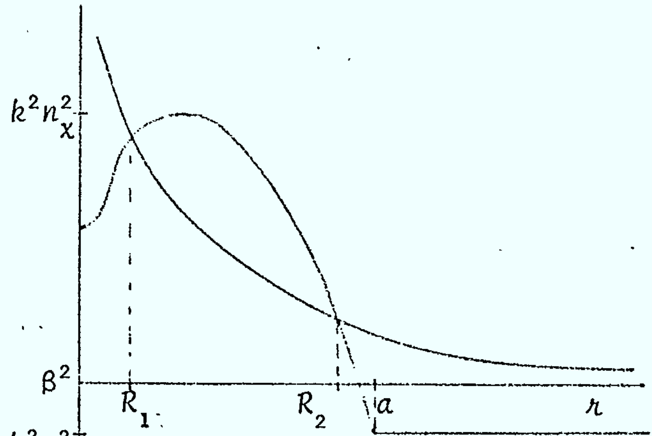

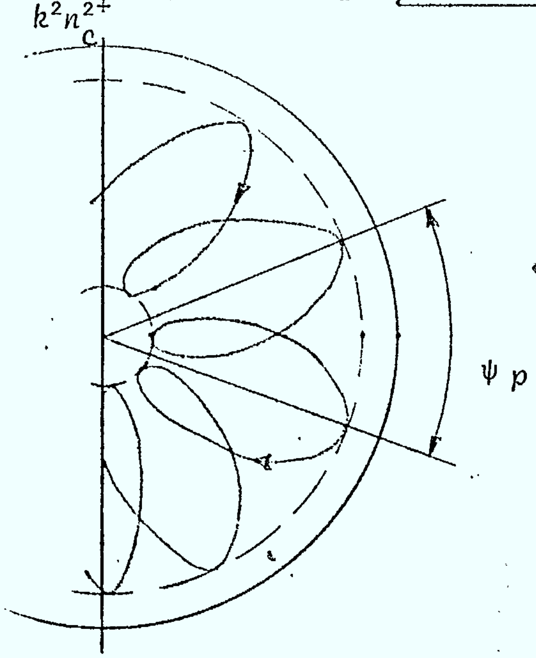

Figure 3.2 Radial Component of the Propagation Vector and Ray Projection Parallel to Fiber Axis Showing the Caustics

Figure 3.2 shows where q(r) is real for an index profile n(r) that has a dip in the center (as often occurs with manufactured profiles). Rays and radially oscillatory fields exist for q real. Figure 3.3 shows the schematic periodic variation of ray radius r(z) with axial position. The axial periodic distance is

$$Z_p = 2\beta \int_{R_1}^{R_2} \frac{dr}{q(r)} \tag{3.1.6}$$

during which the ray oscillates from R_1 to R_2 and back to R_1. At the same time the azimuthal coordinate obeys the pseudoperiodic relation

$$\psi(z + Z_p) = \psi(z) + \psi_p \quad \text{where } \psi_p = 2\nu\int_{R_2}^{R_1} \frac{dr}{r^2 q(r)} \tag{3.1.7}$$

corresponding to precessional ray movement shown in the crosssection of Figure 3.2. These ray oscillations occur in the periodic time

$$\tau_p = \frac{2k}{c} \int_{R_1}^{R_2} \frac{n(r)N(r)}{q(r)}\, dr \tag{3.1.8}$$

where

$$N(r) = n(r) - \frac{\lambda\, dn(r)}{d\lambda} \tag{3.1.9}$$

is the group index.

3.1.2 Modal Delay

The total transit time down the fiber length z is

$$\tau(z) = \tau_p\, z/Z_p \tag{3.1.10}$$

or in terms of the transit time per unit length for a particular mode

$$\tau_{\mu\nu} = \frac{k}{c\beta} \left(\int_{R_1}^{R_2} p(r)q^{-1}(r)dr\right)/\left(\int_{R_1}^{R_2} q^{-1}(r)dr\right) \tag{3.1.11}$$

where $p(r) = (1+D_1)n^2(r)-D_2$.

and D_1 and D_2 are two chromatic dispersion parameters defined by

$$D_1 = -\left(\frac{\lambda}{n_o}\frac{dn_o}{d\lambda} + \frac{\lambda}{2\Delta}\frac{d\Delta}{d\lambda}\right) \tag{3.1.12}$$

and

$$D_2 = -\frac{\lambda n_o d\Delta}{2\Delta\ d\lambda} .$$

In the above expressions the index profile is of the general form

$$n(r)=n_o\sqrt{1-2\Delta g(r)} \tag{3.1.13}$$

where $g(r)=1$ when r is greater than the core radius but is otherwise arbitrary. Furthermore it is assumed that the profile function $g(r)$ is independent of wavelength.

3.1.3 Modal Attenuation

There are three types of modes in a fiber: the bound or guided modes that propagate in principle unattenuated, the leaky modes that are guided but attenuated, and the radiating or non propagating modes.

Rays or modes are 'bound' whenever the region of real $q(r)$ is restricted to the core. This means that the axial wavenumber β lies between the maximum core index value n_x (which need not be at the center) and the minimum value n_c (taken to be that of the cladding in Figure 3.2) i.e.

$$kn_c<\beta<kn_x \tag{3.1.14}$$

and $$0<\nu<r\sqrt{k^2n^2(r)-\beta^2} < rk\sqrt{n_x^2-n_c^2}$$

where the maximum value of ν is determined by the radius $r=R_1=R_2$ where the two caustics merge.

The leaky or 'tunnelling' modes have a radially oscillatory field within a region of the core and at least a second region either in the cladding or in the core. This second region corresponds to a third caustic R_3 where $q(R_3)=0$, where R_3 is finite. Optical tunnelling (and leaky mode attenuation) occurs through the evanescent region between R_2 and R_3 where $q(r)$ is imaginary (see Figure 3.4).

The third caustic is in the cladding, i.e. $R_1<R_2<a<R_3$

when the mode is characterized by

$$(k^2n_c^2-\nu^2/a^2)^{\frac{1}{2}}<\beta<kn_c \tag{3.1.15.a}$$

and

$$0<\nu<ak(k^2n_c^2-\beta^2)^{\frac{1}{2}}. \tag{3.1.15.b}$$

When the index profile is not smooth and exhibits many peaks and troughs the third caustic may be within the core with β possibly greater than kn_c.

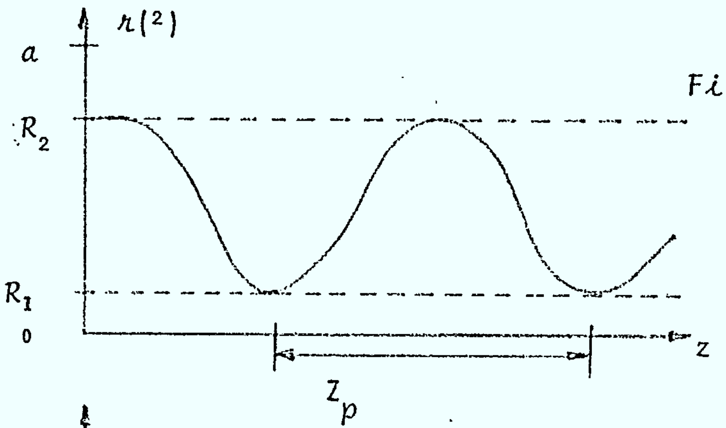

Figure 3.3 Ray Projection on a Meridian Plane of the Fiber Showing the Axial Periodicity.

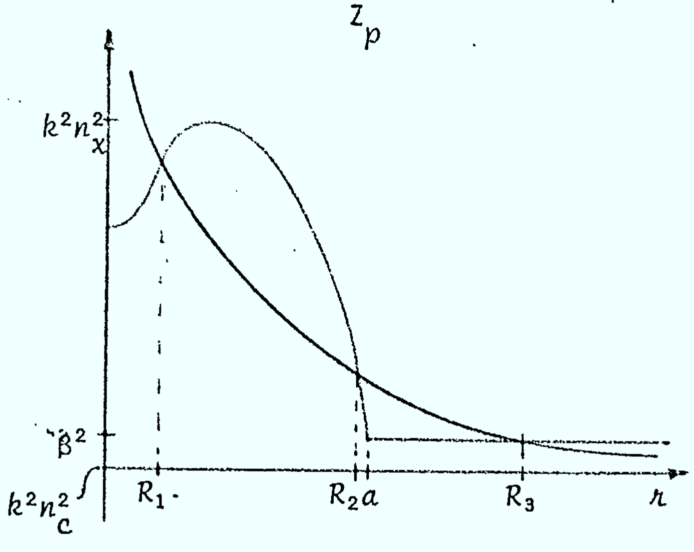

Figure 3.4 Radial Component of the Propagation Vector Showing the Three Caustics of a Leaky Mode.

In between R_2 and R_3, and within R_1 the function $q^2(r)$ is negative valued and the propagation constant is complex, so that, by Eqn. (3.1.4) the fields decay exponentially in the axial z direction. The corresponding power attenuation coefficient is

$$\alpha = \frac{\exp\left(-2k\int_{R_2}^{R_3} |q(r)|\, dr\right)}{Z_p} \qquad (3.1.16)$$

Unbound' or 'radiative' modes correspond to rays that refract into the cladding. These are radially oscillatory everywhere and satisfy

$$k < \beta < \sqrt{k^2 n_c^2 - \nu^2/a^2}$$
$$0 < \nu < a\sqrt{k^2 n_c^2 - \beta^2} < ka\sqrt{n_c^2 - 1} \qquad (3.1.17)$$

3.1.4 Software Implementation

a) Modal Structure

The modal structure of a fiber of cylindrically symmetrical but other-wise arbitrary profile is determined using the WKB model. For all possible positive integers ν, the propagation constant β is recursively set to a value between

$$\beta_{max} = kn_x$$

and

$$\beta_{min} = \sqrt{k^2 n_c^2 - \nu^2/a^2}.$$

The first three roots of $q(r)$ are computed numerically to determine the caustic radii R_1 and R_2 of propagating modes ($0 < R_1 < R_2 < a$) and the third caustic radius R_3 of leaky modes $(R_2 < R_3)$.

Then the integral of $q(r)$ (see Eqn. (3.1.2) is computed between the first two caustics ($r = R_1$ and $r = R_2$). If the integral is equal to $(\mu+0.5)\pi$ where μ is an integer, the chosen β and ν correspond to a propagating or to a leaky mode. If μ is not an integer, values of β corresponding to propagating or leaky modes are found by linear interpolation.

Eventually the process leads to the characterization of each mode by its parameters $\mu, \nu, \beta, R_1, R_2$ and R_3. Cubic spline interpolation is used to obtain the values of the refractive index in between the data points.

b) Modal Delay

The integrals in Eqn. (3.1.11) are evaluated numerically using Simpson's rule except near the caustic radii R_1 and R_2 since these points are poles of the integrands (i.e. $q(R_1) = q(R_2) = 0$).

The contribution of the poles to the integrals can be evaluated by a second order Taylor's expansion of the integrands about the poles. After some algebra the pole contribution is given by

$$\int_{R_i}^{R} p(r)q^{-1}(r)dr = \frac{2p(r_i-r)^{\frac{1}{2}}}{(q^2)'} x$$

$$\left\{1+\frac{r_i-r}{3}\left(\frac{p'}{p}-\frac{(q^2)''}{4(q^2)}\right)+\frac{(r_i-r)^2}{20}\frac{(q^2)''}{(q^2)'}\left(\frac{3(q^2)^2}{8(q^2)'}-\frac{p^1}{p}\right)\right\} \qquad (3.1.18)$$

where the $p, (q^2)'$ and $(q^2)''$ are evaluated at $r=r_i$ and the ' and " stand for first and second derivatives with respect to r. The first and second derivatives are obtained from a cubic spline interpolation of the refractive index profile. This procedure interpolates a function by segments of third degree polynomials which are constrained to have the same first and second order derivative at the data points. Eqn. (3.1.18) can be used as well to evaluate the pole contributions to the denominator of Eqn. (3.1.11) by making $p(r) = 1$ and $p' = 0$ in Eqn. (3.1.18).

The transmit times of individual modes are computed with an accuracy of better than 10 psec/km compared to the analytical solution of a parabolic profile. Figure 3.5 illustrates the close agreement between the computed pulse broadening (RMS) and the exact analytical solution for an α profile fiber. The broken curve shows the case of no chromatic dispersion. The solid curve shows material and profile dispersion corresponding to a TiO_2 doped fiber (i.e. $D_1=0.0774$ and $D_2=0.144$ in Eqns. (3.1.12)).

c) Modal Attenuation

The leaky mode attenuation is computed according to Eqn. (3.1.16) for the values of (β,ν) that are solutions of Eqn.(3.1) with integer μ. When the third caustic is in the cladding ($R_3 \geq a$) advantage is taken of an analytical solution of the integral in the exponent of Eqn. (3.1.16) because then the refractive index is constant and equal to the cladding index:

$$\int_a^{R_3} |q(r)|dr = -\left[A + 0.5\nu \log \frac{\nu-A}{\nu+A}\right] \qquad (3.1.19)$$

where

$$A^2 \equiv \nu^2-a^2(k^2n_c^2-\beta^2).$$

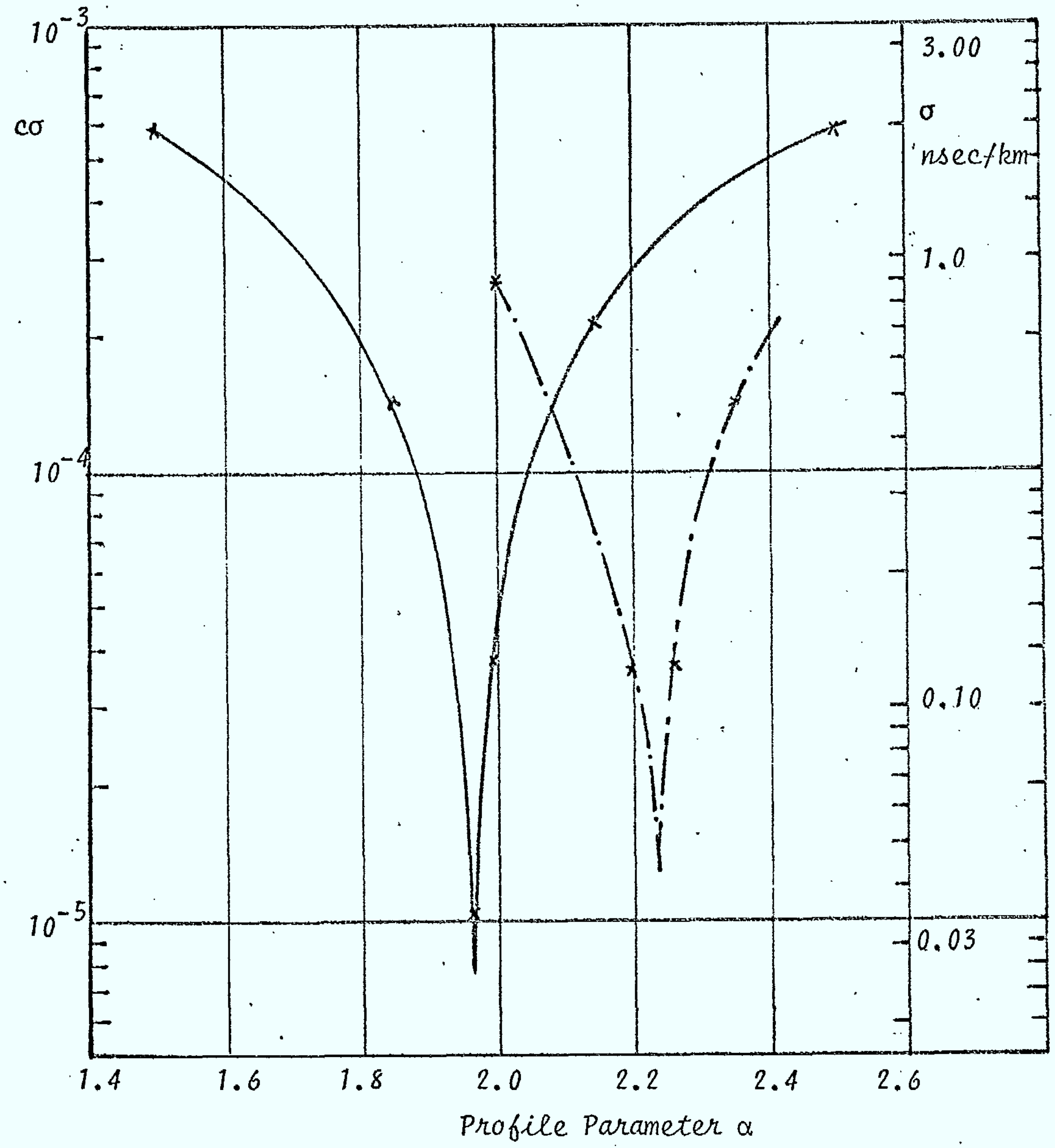

Figure 3.5 Normalized Width of the Impulse Response of a Fiber with Power-Law Index Profile α. The curves represent the Analytical Solution for the Cases of No Chromatic Dispersion (solid line) and of Material and Profile Dispersion of a TiO_2 Doped Fiber (broken line). The x's Indicate the Solutions Computed via the WKB Model.

3.2 Source

3.2.1 Rays Outside the Fiber

Here the curving rays inside the fiber are related to those just leaving (or entering) the endface going as a straight ray into (or out of) a material of index n_a. Only the angle θ is changed according to Snell's law and the ray invariants of Equation (3.1.2) are

$$\beta = k \sqrt{n^2(r) - n^2 \sin^2 \theta(r)} \qquad (3.2.1)$$

$$\nu = k r n_a \sin \theta(r) \cos \phi(r)$$

The (r, θ) quantities are from now on understood to locate straight rays <u>just outside</u> the fiber in the external index n_a.

In terms of external coordinates, the bound ray conditions of Equations (3.1.2) are

$$0 \leq n_a \sin \theta(r) \leq \sqrt{n^2(r) - n_c^2} \qquad (3.2.2)$$
ϕ unrestricted

defining a circular acceptance cone decreasing in angular width as the core/clad interface is approached. The leaky ray conditions of Equations (3.1.15) allow a larger incidence angle satisfying.

$$\sqrt{n^2(r) - n_c^2} \leq n_a \sin \theta(r) \leq \sqrt{\frac{n^2(r) - n_c^2}{1 - \frac{r^2}{a^2} \cos^2 \phi(r)}} \qquad (3.2.3)$$

The acceptance cone is elliptical as in Figure 3.6; the minor axis corresponds to the meridional plane $\phi = \pi/2$. Unbound rays exceed the above upper limit of Equation (3.2.1)

3.2.2 Fiber Near-Field

The power in a given (β, ν) mode is made up of all (r, θ, ϕ) rays satisfying Equations (3.2.2). It can be shown that the power density $P(\mu, \nu)$ in mode (μ, ν) is related to the power density $P(\beta, \nu)$ by

$$P(\mu, \nu) d\mu d\nu = P(\beta, \nu) m(\beta, \nu) d\beta d\nu$$

where

$$m(\beta, \nu) = 4 \left| \frac{d\nu}{d\beta} \right| = 2Z_p/\pi \qquad (3.2.4)$$

is a mode density and Z_p is the axial period of Eqn. (3.1.6). The importance of these relationships, is that $P(\beta,\nu)$ with $\beta=\beta(r,\theta)$ and $\nu = \nu(r,\theta,\phi)$ is directly proportional to the radiance $L(r,\theta,\phi)$ (i.e. power per unit area and solid angle).

Finally, it can be shown that for fibers and radiation patterns that are both circularly symmetric, the near-field distribution (power at the fiber face per unit area as a function of radial position) is given by

$$NF(r) = N_o \int_{kn(\ )}^{kn(r)} \beta d\beta \int_o^{\nu_m} (\nu_m^2 - \nu^2)^{-\frac{1}{2}} \ P(\beta,\nu) d\nu \qquad (3.2.5)$$

where

$$\nu_m(r,\beta) = r(k^2 n^2(r) - \beta^2)^{\frac{1}{2}} \ .$$

and N_o is a constant independent of (r,θ,ϕ) or (β,ν).

3.2.3 Fiber Far-Field

Similarly it can be shown that the far-field distribution (power far from the fiber face per unit solid angle as a function of the angle with the fiber axis) is given by

$$F(\theta) = F_0 \ \cos\,\Theta \int_{kn(a)}^{\beta m} \left(\frac{dn^2}{dr^2}\right)^{-1} \beta d\beta \int_o^{\nu_o} (\nu_o^2 - \nu^2)^{-\frac{1}{2}} P(\beta,\nu) d\nu \qquad (3.2.6)$$

where

$$\nu_o(r,\theta) = kr \sin\theta$$

$$\beta_m(\theta) = k(n^2(o) - n_o^2 \sin^2\theta)^{\frac{1}{2}}$$

$$r = r(\theta,\beta)$$

and F_o is a constant independent of (r,θ,ϕ) or (β,ν).

3.2.4 Modal Power Distribution

The power in the fiber modes $P(\beta,\nu)$ appears in both the near-field Equation (3.2.5) and the far-field Equation (3.2.6). However, it does not appear possible to invert these expressions to solve for the modal power distributions in terms of the near-field or far-field or both.

If the approximate assumption that the modal power distribution is independent of ν is made, then

$$P(\beta) = P_o \left|\frac{dNF/dr}{dn^2\ /dr}\right|_{r_o} \qquad (3.2.7)$$

where $n(r_o) = \beta$.

Then only the near-field pattern and refractive index profile need to be differentiated.

Another potential method of finding $P(m,\nu)$, related to $P(\beta,\nu)$ by Equation (3.2.4) is to superpose the modal powers as

$$NF(r) = \sum_{\mu,\nu} P(\mu, \nu) \; |E_{\mu,\nu}(r)|^2 \tag{3.28}$$

where the fields are the WKB solution of Equation (3.1.4). With NF measured and E calculated, the $P_{\mu,\nu}$'s can be solved for.

3.3 Joints

The joint model is based on geometrical optics. The incoming and outgoing rays are described in terms of the modal parameters of the fiber.

3.3.1 Geometrical Optic Model

The model determines the matching conditions under which an incoming ray of the transmitting fiber is converted into an outgoing ray of the receiving fiber. The matching conditions are Snell's law and the law of continuity of the planes of incidence and refraction.

The two fibers are characterized by their

- radii a_i $(i=1,2)$ and
- index profiles $n_i(x_i) = n_{oi} \sqrt{1-2\,\Delta_i g_i(x_i)}$ $(i=1,2)$ (3.3.1)

where x is the radial coordinate in fiber i normalized with respect to a_i. The transmitting fiber is refered to by the subscript i=1 while i=2 corresponds to the receiving fiber.

a) Snell's Law

For any point on the overlap area of the two cores, Snell's law relates the angle of refraction to the angle of incidence.

$$n_1(x_1) \sin \Theta_1 = n_2(x_2) \sin \Theta_2 \tag{3.3.2}$$

where Θ_1 and Θ_2 are the angles inside the fiber made by the incident and refracted rays respectively with the fiber axis (see Fig. 3.7). Then a relation between the propagation constants of the incoming and the outgoing modes can be determined. With the normalized notation

$$\beta_i^2 = k^2 n_{oi}^2 (1-2\Delta_i b_i) \quad (i=1,2) \tag{3.3.3}$$

and with Eqn. (3.3.1), Eqn. (3.3.2)

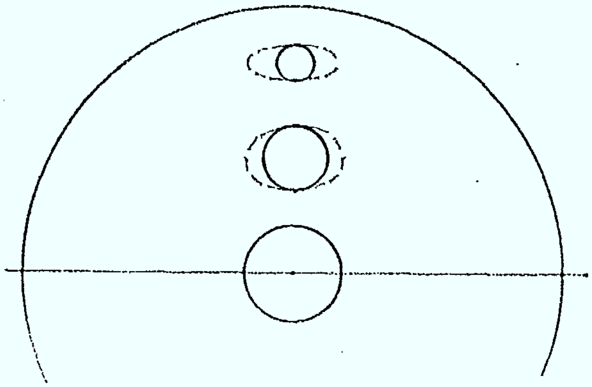

Figure 3.6 Crosssection of the Cone of Light Acceptance at Various Points along the Fiber Radius. The Solid Lines Correspond to Propagating Modes. The Dotted Lines correspond to Leaky Modes.

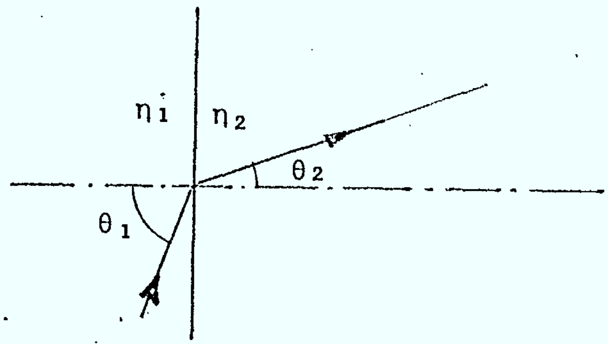

Figure 3.7 Snell's Law of Refraction

$$b_2=g_2(x_2)+(a_2/a_1)(V_1/V_2)^2(b_1-g_1(x_1)) \qquad (3.3.4)$$

where the V_i's are the V numbers of the fibers

$$V_i= kn_{oi}a_i\sqrt{2\Delta_i} \ . \qquad (i=1,2) \qquad (3.3.5)$$

Eqn. (3.3.4) is the matching condition between the normalized propagation constant of the incoming and outgoing modes. The right hand side of Eqn. (3.3.4) is totally determined for any point of the overlap area and for an incoming mode. If it is not equal to the propagation constant of a mode in the receiving fiber the ray at x_i does not transfer any power into a propagating or leaky mode of the receiving fiber.

In Eqn. (3.3.4) x_1 and x_2 are the radial coordinates of a unique point with respect to the center of the two fibers. They are related by

$$x_2^2 = (a_1/a_2)^2(x_1{}^2+ \varepsilon^2-2\varepsilon x_1 \cos \psi) \qquad (3.3.6)$$

where the transverse offset d is normalized with respect to a_1

$$\varepsilon=d/a_1 \qquad (3.3.7)$$

and ψ is the azimutal coordinate of the point with respect to the transmitting fiber (see Fig. 3.8).

b) Continuity of the plane of incidence

The incident ray, the refracted ray and the normal to the fiber end face must all lie within a same plane. This continuity of the plane of incidence imposes that the projections of the propagation vectors of the transmitting and receiving fiber on a plane normal to the fiber axis be colinear (i.e parallel). This is equivalent to a matching condition on the azimuthal parameter ν of the incoming and outgoing modes.

Figure 3.8 shows the projections of the propagation vectors of mode h in the transmitting fiber (j=1) and of mode i in the receiving (j=2). These projections make an angle ϕ_{tj}(t=k,i) with the radius extending from the common point in the area of core overlap to the center of the transmitting and receiving fiber. The parameter ν of mode t is given by

$$\nu_{tj}=x_jV_{tj}\sqrt{b_{tj}-g_{tj}(x_j)} \sin \phi_{tj}. \qquad \begin{matrix} j=1,2 \\ t=h,i \end{matrix} \qquad (3.3.8)$$

A matching condition at the point x_1(or x_2) between an incoming and an outgoing mode exists when Eqn. (3.3.8) has two simultaneous solutions ν_{h1} and ν_{i2} where

$$\phi_{i2}=\phi_{h1}+ \omega$$

in which ω is a solution of

$$\varepsilon^2= x_1^2+x_2^2(a_2/a_1)^2-2x_1x_2(a_2/a_1) \cos \omega. \qquad (3.3.9)$$

3.3.2 Software Implementation

The software model has the capability to handle transmitting and receiving circular fibers of same or different radii, index profiles and numerical apertures. The two fibers can be transversally misaligned. The determination of matching conditions is done repeatedly for all points in the overlap area of the cores. This area is one of three types dependent upon the relative values of the radii and the transverse offset:

a) if $0<\varepsilon<|1-a_2/a_1|$: no intersection of core circumferences (see Fig. 3.9.a)

b) $|1-a_2/a_1|<\varepsilon|1-(a_2/a_1)^2|^{\frac{1}{2}}$: both centers are on the same side of the chord joining the intersection points of the core circumferences (see Fig.3.9.b)

c) $|1-(a_2/a_1)^2|^{\frac{1}{2}}<\varepsilon$: the centers are on opposite sides of the chord. (see Fig.3.9.c)

3.3.3. Crosscoupling Example

Figure 3.10 shows an example of crosscoupling corresponding to the same fiber as both the transmitting and the receiving fiber with a relative offset ε=0.2. The columns of this matrix correspond to the incoming modes. The rows correspond to the outgoing modes. The matrix elements indicate how many points of the area of core overlap satisfy matching conditions (3.3.6) and (3.3.8) between an incoming mode and an outgoing mode. The blank spaces are equivalent to zero matching points. The power weighting at all these points is not included in this result. The figure shows that in the particular example chosen, the crosscoupling is predominantly to adjacent modes when the modes are ordered by increasing b (i.e. decreasing β), and that the crosscoupling window also expands as b increases. For a perfect joint, i.e. identical fibers with no relative offset, a diagonal matrix would have been observed.

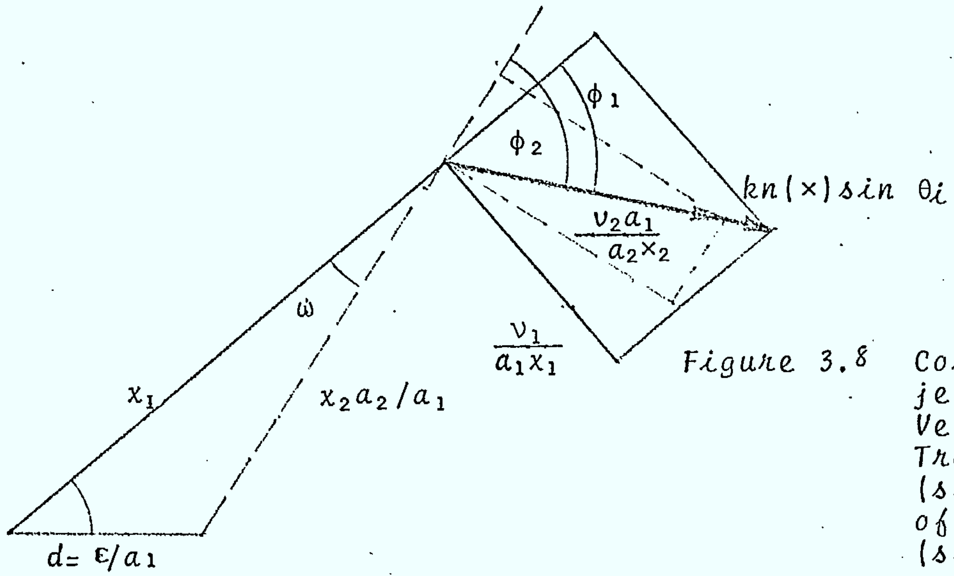

Figure 3.8 Colinearity of the Projections of the Propagation Vectors of a mode of the Transmitting Fiber (subscript 1) and a mode of the Receiving Fiber (subscript 2)

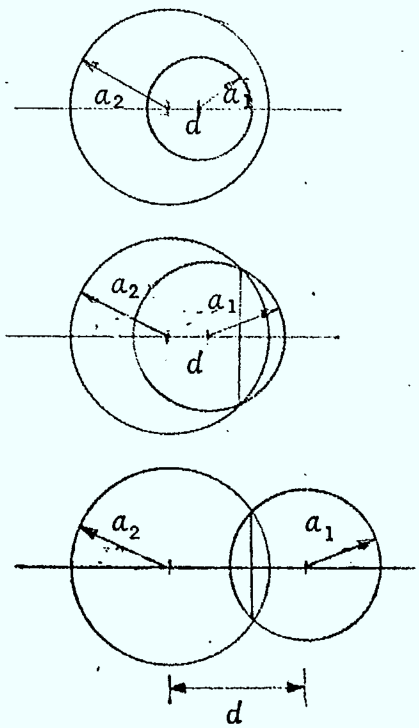

Figure 3.9 Configuration of Core Overlap in Joint Model:

a) no intersection of core circumferences

b) both centers are on the same side of the chord joining the intersection oints of the core circumferences.

c) the centers are on opposite sides of the chord

Figure 3.10 Mode Coupling at a Joint. Relative Transverse Offset = 0.2 Identical Transmitting and Receiving Fibers. The Numbers Indicate How-Many Points of the Core Overlap Correspond to a Match Between an Incoming Mode (Horizontal) and an Outgoing Mode (Vertical).

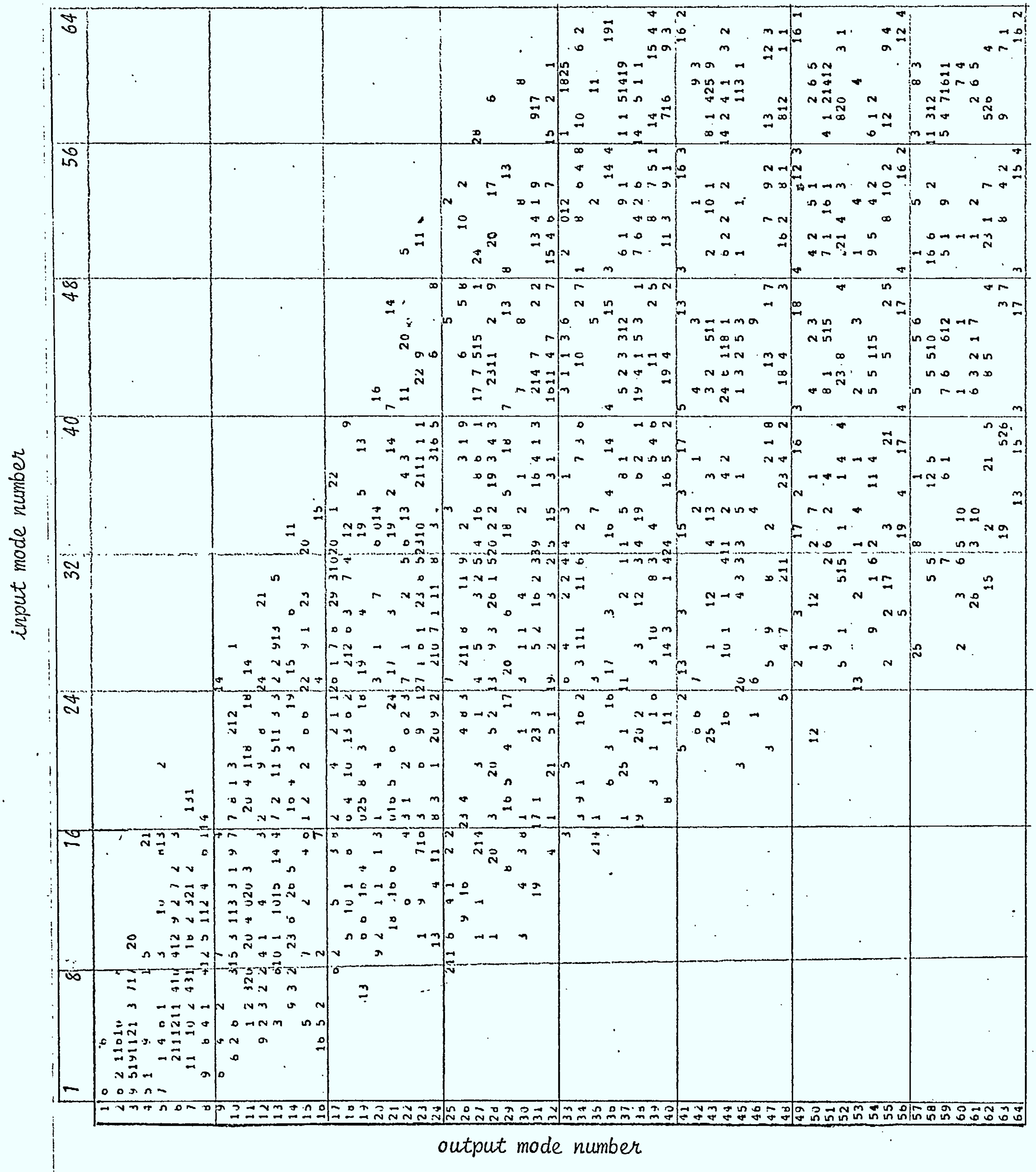

4. Experimental Aspects of the Model

4.1 Measurement of the Near-Field Pattern

The following is a brief description of the experimental techniques used in this project for the measurement of the near- and far-field intensity distributions of a graded index ($\alpha \cong 2$) fiber. The near-field pattern is of particular interest in that from it, one can obtain the refractive index profile of the fiber under study.

A schematic of the experimental apparatus is shown in Figure 4.1. The source is an LED operating at a centre wavelength of 839 nm (FWHM = 48 nm), which is bonded to a 3 metre length of step index fiber. One end of the graded index fiber to be measured is fusion-spliced to this step index fiber while the other end is mounted in a vacuum chuck after cleaving. The cladding light is stripped from the fiber by soaking a jacketless length of fiber (approx. 4 cm) in index matching fluid. For the near field intensity distribution, a magnified image of the fiber output face is focussed onto the active area of a CCPD (Charge Coupled Photodiode) device which consists of 1024 silicon sensor elements on 16 μm centres. The detector response is fed into a digital processing oscilloscope (DPO) where the entire power profile can be viewed and, if necessary, optimized. Such optimization as focussing and image location is achieved by means of the stacked XYZ translation stages to which the vacuum chuck is attached. The digitized signal is then directed to a Tektronix 4052 computer through the standard GPIB interface bus. Figure 14 shows a beam splitter in use to direct the near-field image to the CCPD array. This allows the user to simultaneously view the fiber face on a ground glass screen and therefore to correct improper end preparation. The imaging region is encased in a camera to allow photographs of the fiber face to be recorded. From these, the core and cladding diameters can be measured.

4.2 Measurement of the Far-Field Pattern

The far-field pattern, which is a measure of the angular distribution of light intensity away from the face of the fiber, is also detected using this apparatus. A sliding mirror is moved into position between the output face and the first magnifying objective in order to deflect the far-field image onto a second detector array. As before, the signal is displayed on the DPO and directed to the computer for further processing. Knowing the magnification at the plane of the detector, one can calculate the numerical aperture of the fiber.

4.3 Measurement of Differential Mode Attenuation and Delay

The experimental set-up for measuring differential modal delays and attenuation is shown in Fig. 4.2. A semiconductor laser diode, operating at 0.83 μm and modulated by a 250 MHz sinusoid, is coupled to a single-mode fiber. The free end of the single-mode fiber and one end of the test (multimode) fiber are then brought into close proximity (~ 100 μm apart) and the fiber axes are carefully aligned. Different mode groups of the multimode fiber are excited by laterally translating the single-mode fiber across a common diameter. The light emanating from the output end of the test fiber is collected by an optical receiver connected to the measuring arm of a vector voltmeter. In its reference arm, a small fraction of the modulating sinusoid is fed to serve as a reference for the measurement of the phase delay associated with each mode group (assuming weak intermodal coupling) of the multimode fiber.

The laser diode is biased well above its threshold current and the 250 MHz, 10 mA(p-to-p) sinusoidal current is superposed to produce a modulation index of 50%. The optical level is kept approximately constant by carefully controlling both the temperature of the laser and the bias current via separate feedback loops. Indeed no variation in the laser power level larger than 0.05 dB was observable after a warm-up time of approximately one hour.

Near-field and far-field scans, taken after immersing the single-mode fiber in stripping oil, established both the N.A. (~0.10) and the spot-size (~7μm) of the approximately circularly symmetric probe. Accurate translation of the single-mode fiber at the input end of the test fiber is achieved by a Burleigh Inchworm Translator System (PZ505 & PZ550). This makes possible smooth translations at speeds as low as 1 μm/sec with an overall resolution of approximately 2μm.

The light output from the test fiber is focussed on an APD (RCA 30902 E) with a rather large sensitive area of 0.2 mm^2 and a rise and fall time of about half a nanosecond. A transimpedance amplifier increases the signal to a useful level (~ 75 dB gain) before feeding it into the vector voltmeter. The response of the optical receiver is flat over its 300 MHz bandwidth. The SNR at 250 MHz and 50% modulation index was measured to be better than 70 dB.

For the modulation frequency employed, i.e. 250 MHz, the modal group delay time (assuming negligible mode conversion) is given by ($\Phi/90 \times 10^9$) seconds, where Φ is the phase delay measured in degrees relative to the reference signal. Since the resolution of the vector voltmeter is approximately 0.5 degrees, the time resolution is about 5 picoseconds. Relative amplitude measurements can be made to within ± 2% or 0.25 dB by changing the modulation signal to 100 MHz.

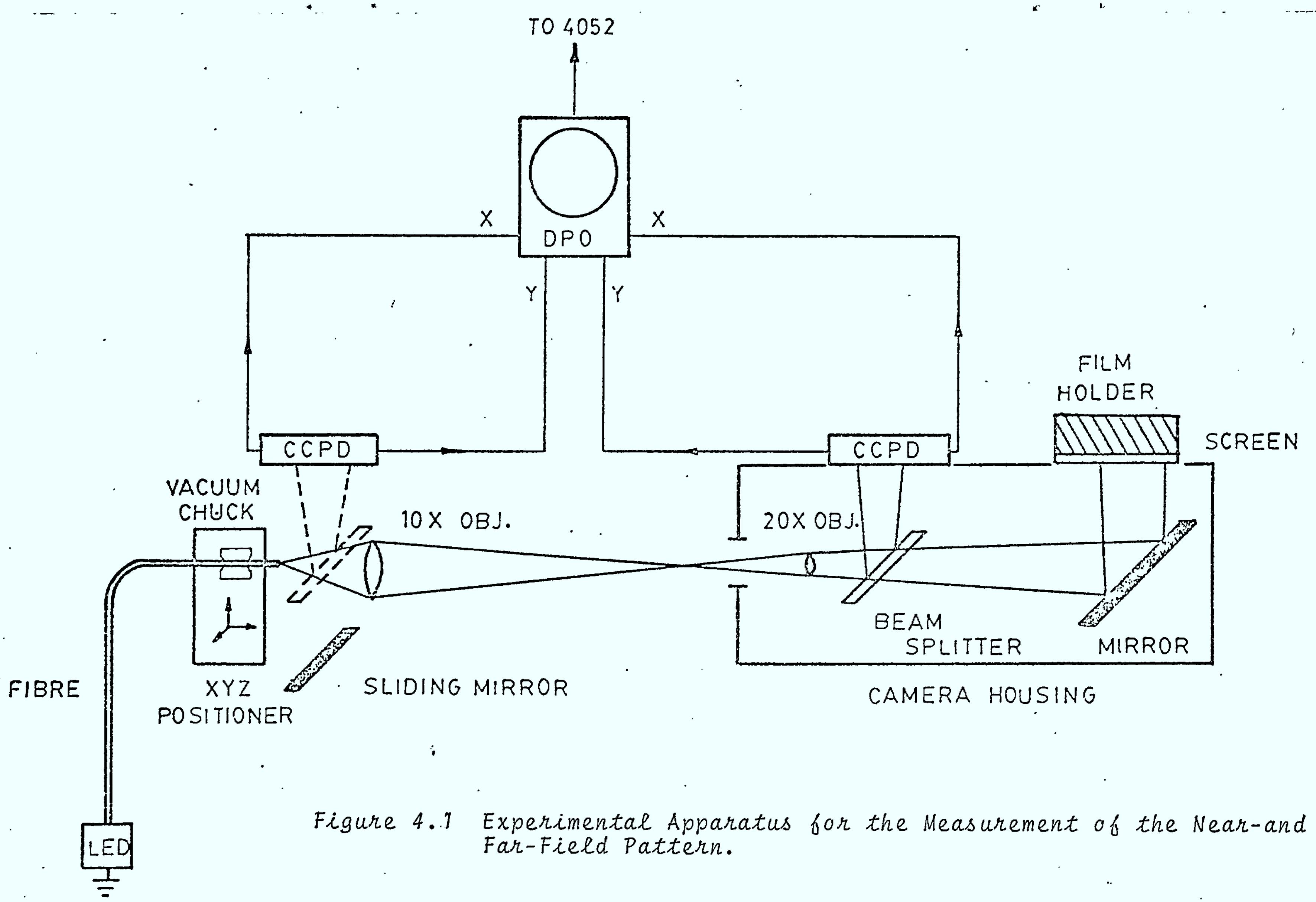

Figure 4.1 Experimental Apparatus for the Measurement of the Near-and Far-Field Pattern.

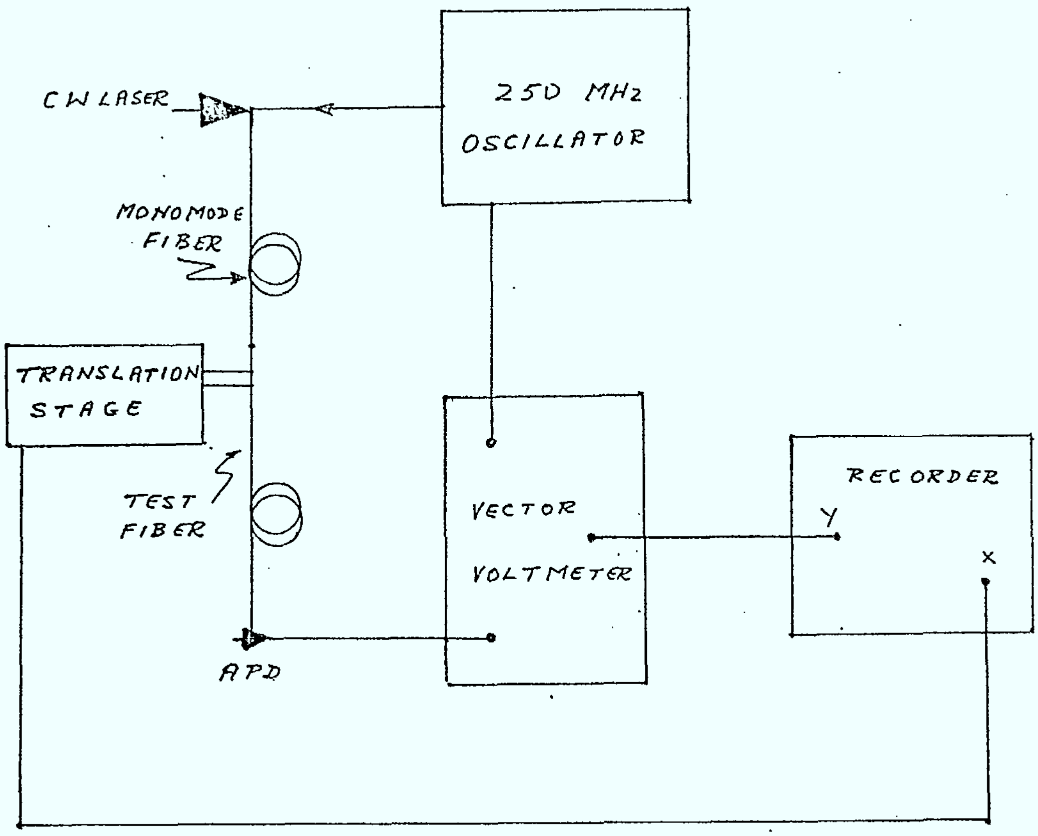

Figure 4.2 Experimental Apparatus for Measuring Differential Mode Attenuation and Delay

5. THEORETICAL AND EXPERIMENTAL RESULTS

5.1 Baseband Response of a Fiber Section

The baseband response of a 656 m section of fiber has been characterized using three different approaches, namely

a) a time domain measurement of the impulse response,
b) a computation based on the measured index profile, and
c) a computation based on the measured differential mode attenuation and delay.

5.1.1 Baseband Response from Time-Domain Measurement

Figure 5.1 illustrates the impulse response of the fiber section obtained from a deconvolution of the input and output pulses. This response has a full width at half maximum (FWHM) of 1.16 nsec and a full width RMS (FWRMS) of 1.04 nsec.

5.1.2 Baseband Response Calculated from Index Profile Measurement

a) Index Profile

Figure 5.2 shows the index profile of the same fiber. It was obtained using the method discussed in Section 4.1. The characteristics of the profile are:

cladding index: 1.4560
maximum NA : 0.157
nominal NA : 0.160
core diameter: 50 μm

On the profile the core-cladding boundary is taken as the 5% point on the right-hand side. The core center is taken at the peak of the secondary lobe within the central depression.

The right hand side of the profile was used in the WKB computation of the mode characteristics. The WKB model was used to determine the mode structure of the fiber and the transit time of its modes.

The impulse response is obtained as a weighted sum of the power carried by all the modes whose transit times fall within a 0.3nsec time slot. The weighting factor is 4 for modes with $\nu \neq 0$ to account for the four-fold degeneracy caused by two possible polarizations and a sine or cosine azimuthal dependence. The weighting factor is 2 for modes with $\nu=0$ since they have no azimuthal degeneracy.

Figure 5.1 Experimentally Measured Impulse Response of the Test Fiber (656 meter long).

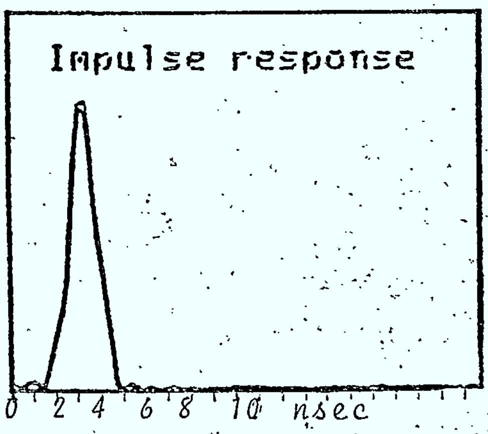

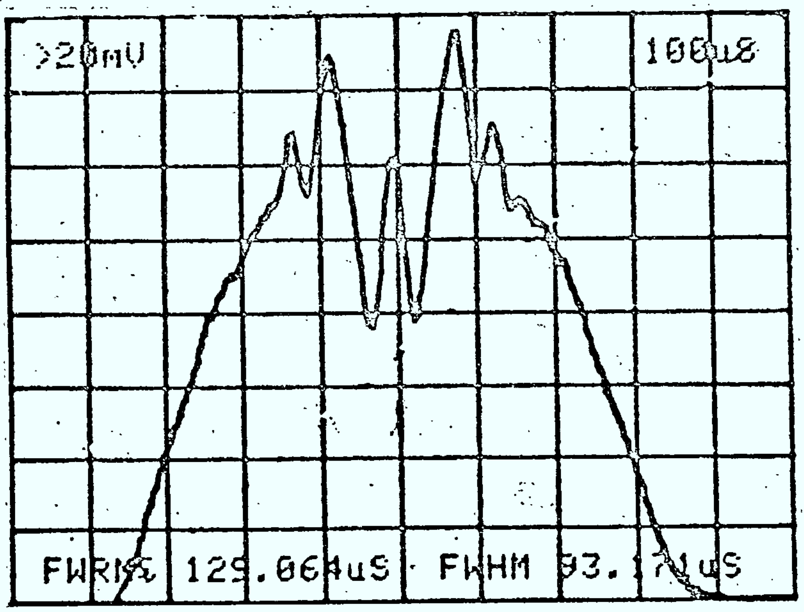

Figure 5.2 Experimentally Measured Index Profile of the Test Fiber.

b) Launching Conditions

The impulse response depends both on the modal characteristics of the fiber and the modal power distribution (MPD) at its input end. The impact of MPD on the impulse response is illustrated in Figure 5.3. The MPD is assumed to correspond to a launch beam of varying spot size (SS) and numerical aperture (NA_L). For a given SS and NA_L, the mode (μ,ν) of the fiber is included in the impulse response when its propagation constant is greater than the limiting β_L corresponding to the launch beam NA_L.

$$\beta_{\mu\nu} \geqslant \beta_L = n_o k(1-2\Delta(NA_L/NA)^2)^{\frac{1}{2}}$$

and when its inner and outer caustics are both contained within the area of the spot size of radius R_{ss}:

$$R_1(\mu,\nu) \leqslant R_2(\mu,\nu) \leqslant R_{ss}.$$

The above conditions are taken as sharp excitation boundaries. All modes that satisfy them are counted in the impulse response with a weight of 2 or 4 depending on ν. All other modes are not counted in the impulse response. The modes are otherwise assumed equally attenuated and not coupled.

Figure 5.3 indicates the variation of the pulse broadening (FWRMS(a); FWHM(b)) as a function of SS and NA_L. The diameter of the SS is expressed in percentage of the core diameter. NA_L is expressed in percentage of the fiber NA.

Figure 5.3 shows that the SS and NA_L are not totally independent constraints as the FWRMS or FWHM can be constant for a given NA_L when the spot size is varied. This means that the NA_L constraint excludes modes that correspond to the larger SS.

For the fiber analysed, pulse broadening does not vary monotonically with SS or NA_L. With near-optimum fibers, the transit times of all modes are almost equal but the transit time of higher or lower order modes are spread more or less randomly within a narrow time interval. Therefore, a change of excitation conditions alters the distribution of modes in a rather random fashion. With over (under) compensated fibers, the exclusion of higher order modes would suppress the fastest (slowest) modes and pulse broadening would vary in a more monotonic fashion.

The information of Figure 5.3 is presented in a pseudo mode volume approach in Figure 5.4. The relative mode volume is defined here by

$$MV = \frac{(SS)^2 x (NA_L)^2}{(\text{core diameter})^2 x (NA)^2}$$

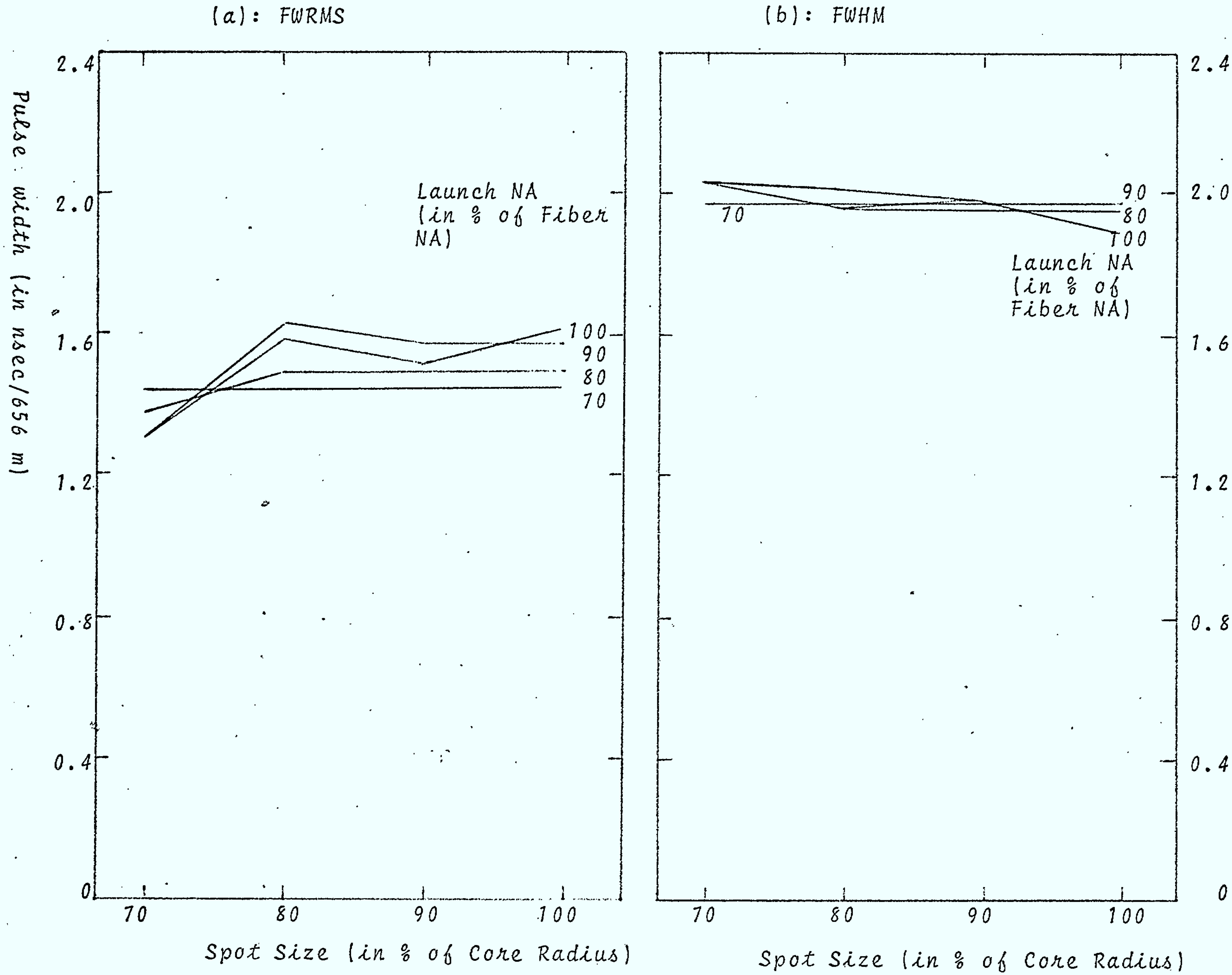

Figure 5.3 Computed Dispersion of the Test Fiber as a Function of Launch NA and Spot Size (a: FWRMS; b: FWHM)

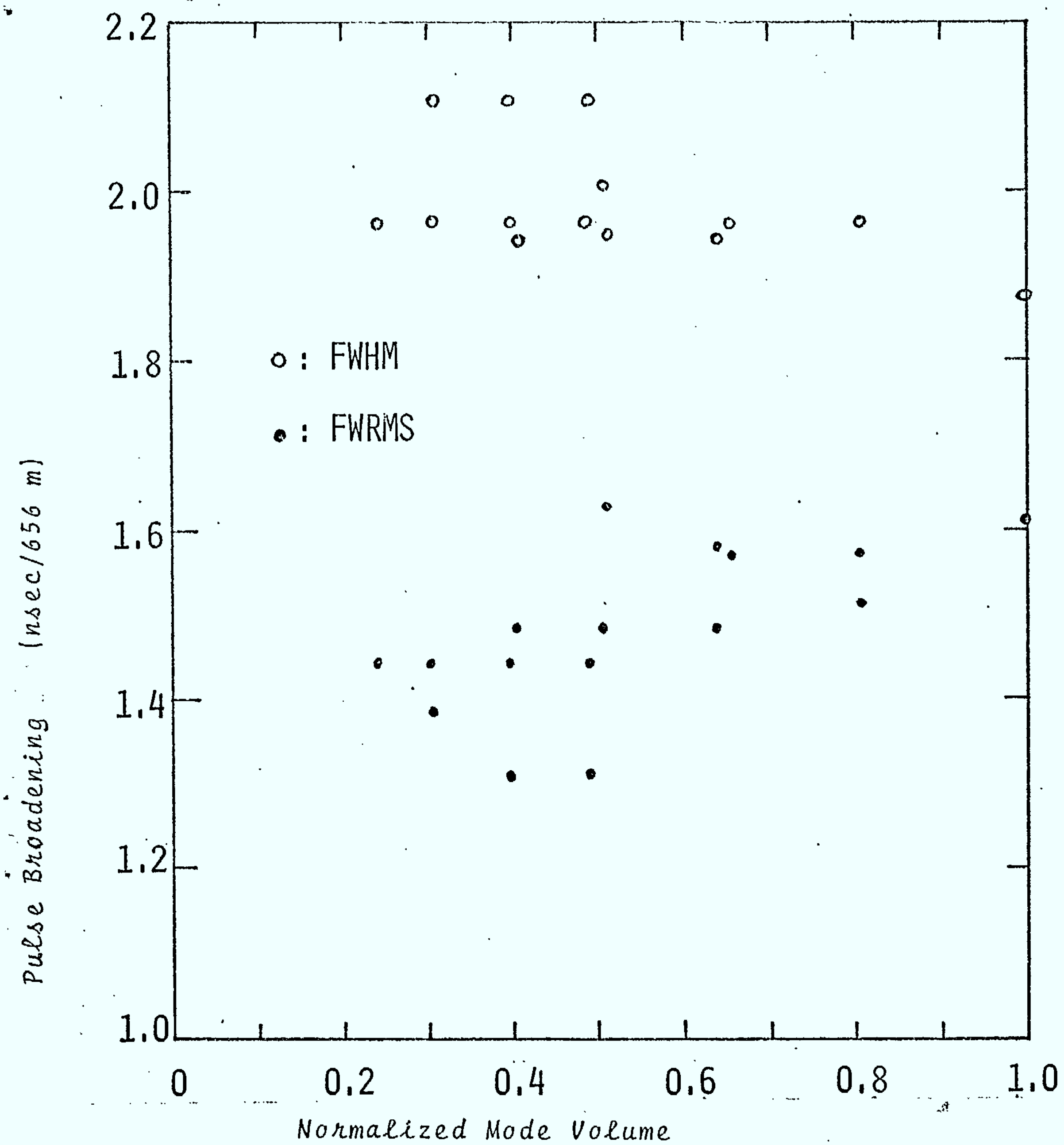

Figure 5.4 Computed Dispersion of the Test Fiber in Terms of Simulated Mode Volume.

Figure 5.4 is a scatter diagram of the FWRMS and FWHM versus MV. For a given mode volume, the spread in FWRMS for the fiber analysed is up to +/- 25% about an average value.

Figure 5.5 illustrates the change in power carried by the fiber when the beam size and NA_L are reduced from their full value. A NA_L of 80% and a SS of 80% excites 6dB less power than the full beam size and NA.

Figure 5.6 shows the impulse reponse of the fiber for three combinations of SS and NA_L: (100% SS, 100% NA_L), (90% SS, 90% NA_L) and (80% SS, 80% NA_L). The corresponding dispersion parameters are

Spot Size %	NA_L %	FWRMS nsec	FWHM nsec
100	100	1.603	1.874
90	90	1.576	1.968
80	80	1.488	1.945

Table 5.1 Pulse Broadening of the Test Fiber as Computed by the WKB Model for Different Launching conditions.

These pulses are wider than the experimentally measured impulse response. The modal power distribution at the input of the fiber in the measuring apparatus is not exactly known. However, because the fiber is excited via a long length of fiber which acts as a mode mixer as well as via a mode stripper, the input excitation is likely to correspond to a reduced beam excitation. The 80% SS-80% NA_L curve of Figure 5.6 has the closest FWRMS but its multipeaked shape is quite different from the experimental impulse response. The addition of differential attenuation and mode coupling would likely help in reducing the pulse width and smoothing out the shape.

The simulation of leaky modes reveals that they hardly affect the impulse response. Only a few leaky modes have an attenuation less than 10dB/km.

5.1.3 Baseband Response Calculated from Differential Mode Measurement

a) Differential Mode Attenuation (DMA) and Delay (DMD)

The impulse response is now determined from the differential mode characteristics obtained with the set-up described in Section 4.3. Figures 5.7 and 5.8 show the differential attenuation and delay obtained as the difference (in dB and nsec respectively) between the measurements at the output of a long and a short length of the fiber when the launching single-mode fiber is moved along a radius at the input end. This fiber is the same as that used in Sections 5.1.1 and 5.1.2.

Figure 5.7 indicates how the light launched at a given radius is attenuated over 653 meters. (A 3 meter length was cut off the initial 656m in order to measure the power launched inside the test fiber by the monomode fibre). Similarly Figure 5.8 indicates the relative transit time of the light launched at the same radius.

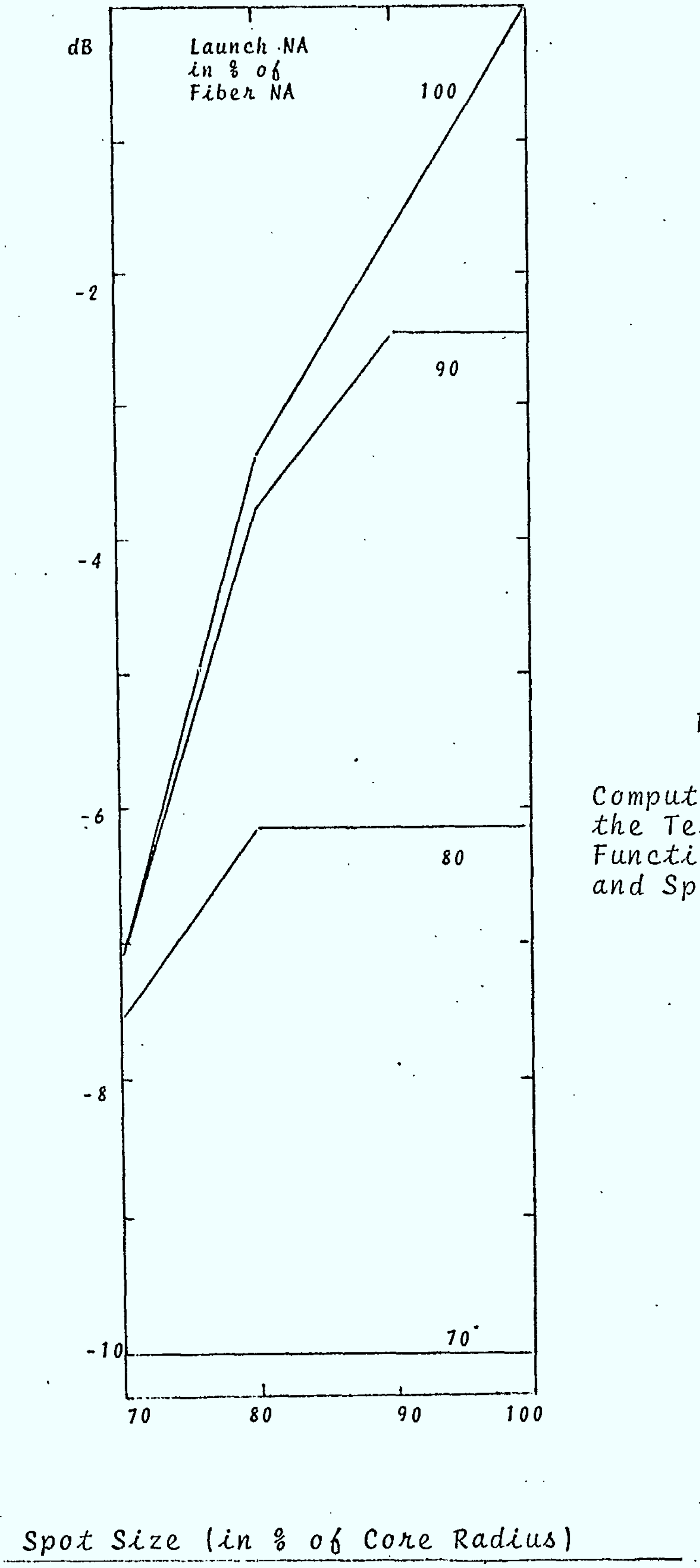

Figure 5.5

Computed Power Guided by the Test Fiber as a Function of Launch NA and Spot Size

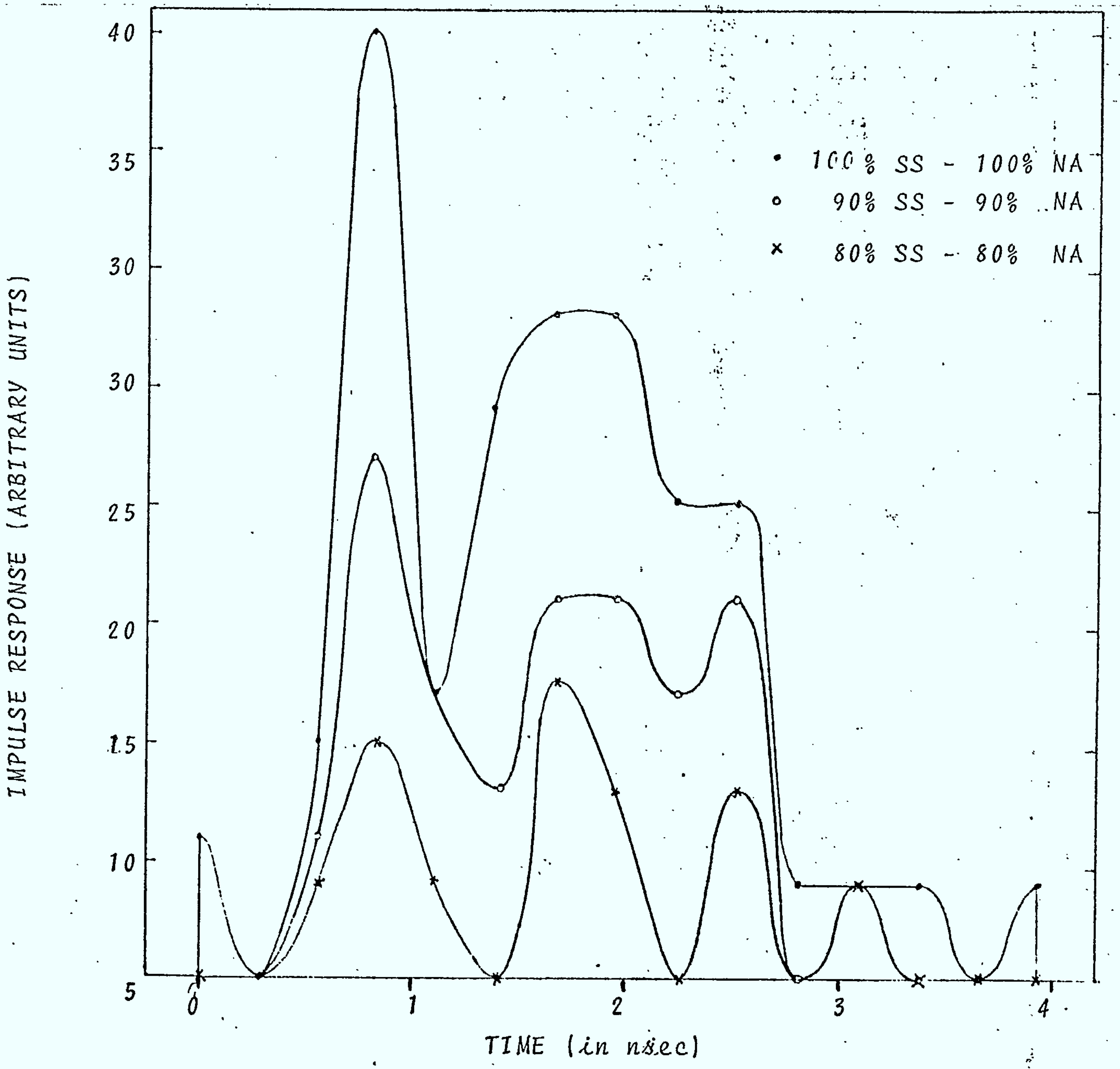

Figure 5.6 Impulse Response of the Test Fiber as a Function of the Launch NA and Spot Size

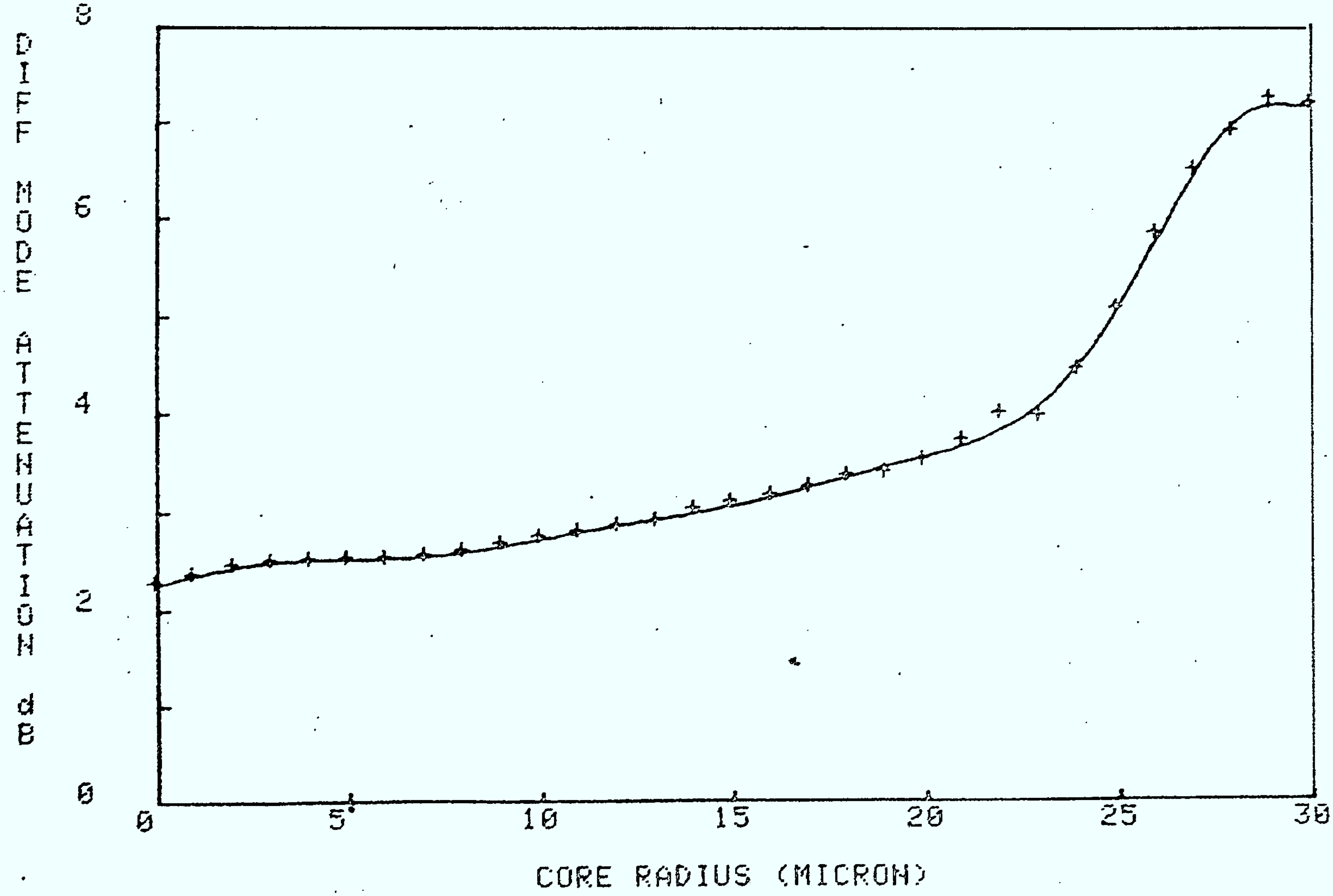

Figure 5.7 Measured Attenuation of the Test Fiber as an Function of the Radial Position of the Launch Monomode Fiber.

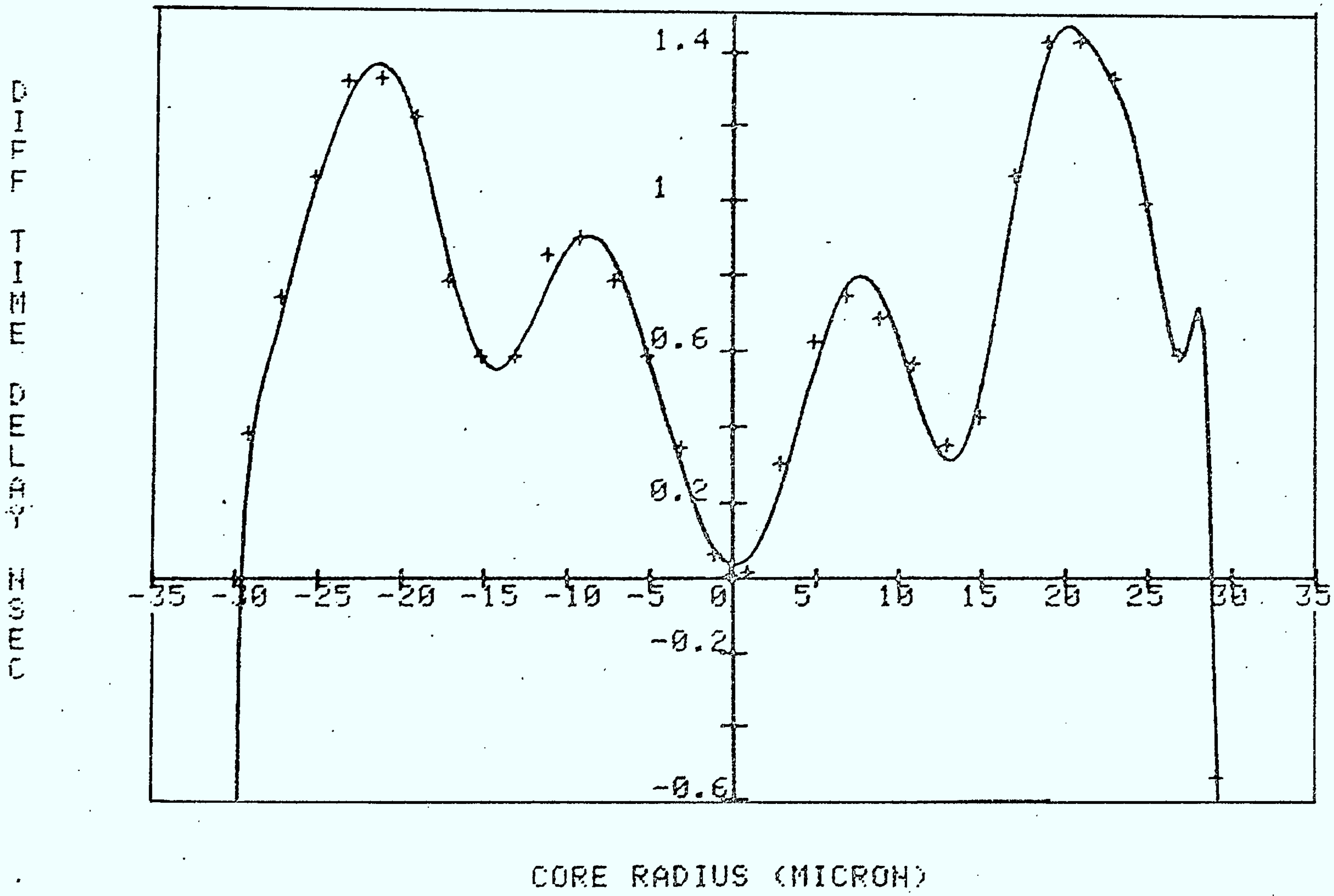

Figure 5.8 Measured Delay of the Test Fiber as a Function of the Radial Position of the Launch Monomode Fiber.

b) Algorithm for the Impulse Response

The impulse response s(t) is obtained by combining the differential mode characteristics as follows:

$$s(t,t+\tau)=cte \sum_{r} rp_{in}(r)10^{-0.1\alpha(r)} \qquad (5.1)$$

where τ is the time resolution of the response, $\alpha(r)$ is the attenuation in dB at the radius r and where the sum extends over all radius positions where the delay $\sigma(r)$ is between t and $t+\tau$.

$$t \leq \sigma(r) \leq t+\tau$$

The coefficient r in Eqn. (5.1) reflects the circular symmetry (area of annulus) of the fiber.

c) Input Power

$p_{in}(r)$ represents the power at radius r on the fiber input face. This power should represent the power distribution or the near-field pattern of the source (in the wide sense) used in the baseband response measurement. To represent it, a few input power functions have been tested. They are illustrated in Figure 5.9 and given by:

$$p_{in}(r) = (1-(r/a)^u)\,(1-p_o \exp(-r^2/2a^2\sigma_o^2))$$

With $u=\infty$ and $p_o=0$ the input power is uniform across the radius (curve a). With $u=2$ and $p_o=0$ the input power is parabolic (curve b).

With $u=2$, $p_o=0$ and $\sigma=0.1$ (curve c) or 0.2 (curve d), the input power is parabolic but distorted by a central depression. This case is meant to simulate a common near-field pattern.

d) Impulse Response

The impulse reponses corresponding to the above data are shown in Figure 5.10. The time resolution has been set to 0.29 nsec to match that of the baseband response apparatus. The overall pulse width is 1.45 nsec and the FWRMS and FWHM are listed below:

Power Distribution	Profile Parameter u	Dip Depth p_o	Dip Width σ_o	FWRMS nsec	FWHM nsec
uniform	∞	0	-	0.77	1.10
parabolic	2	0	-	0.72	0.96
parabolic	2	0.5	0.1	0.72	0.95
with central dip	2	0.5	0.2	0.73	1.01

Table 5.2 Pulse Broadening of the Test Fiber as Computed from the Differential Mode Characteristics under Various Input Power Conditions.

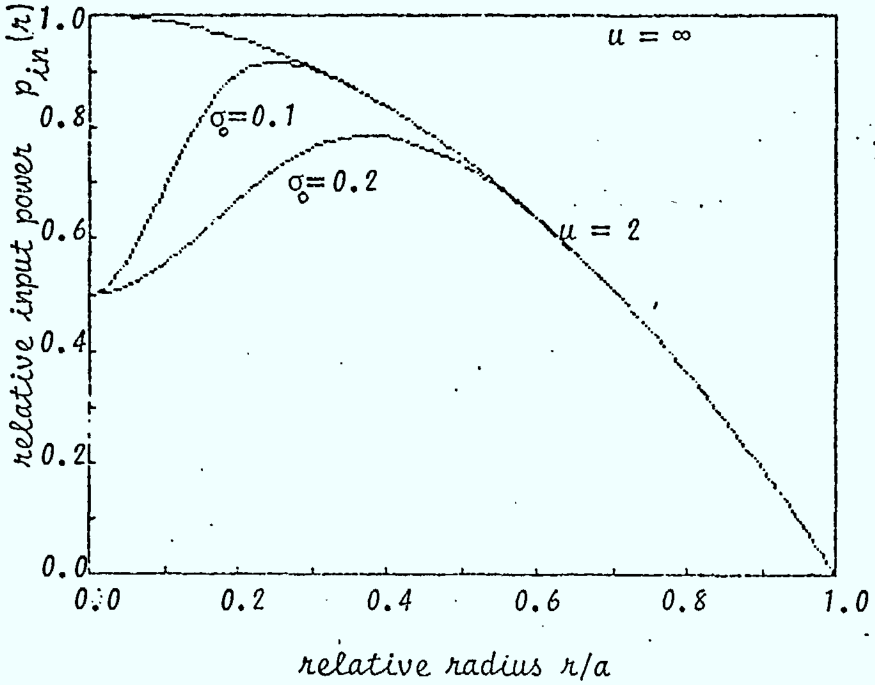

Figure 5.9

Simulated Launch Power as a Function of the Radial Position of the Launch Monomode Fiber.

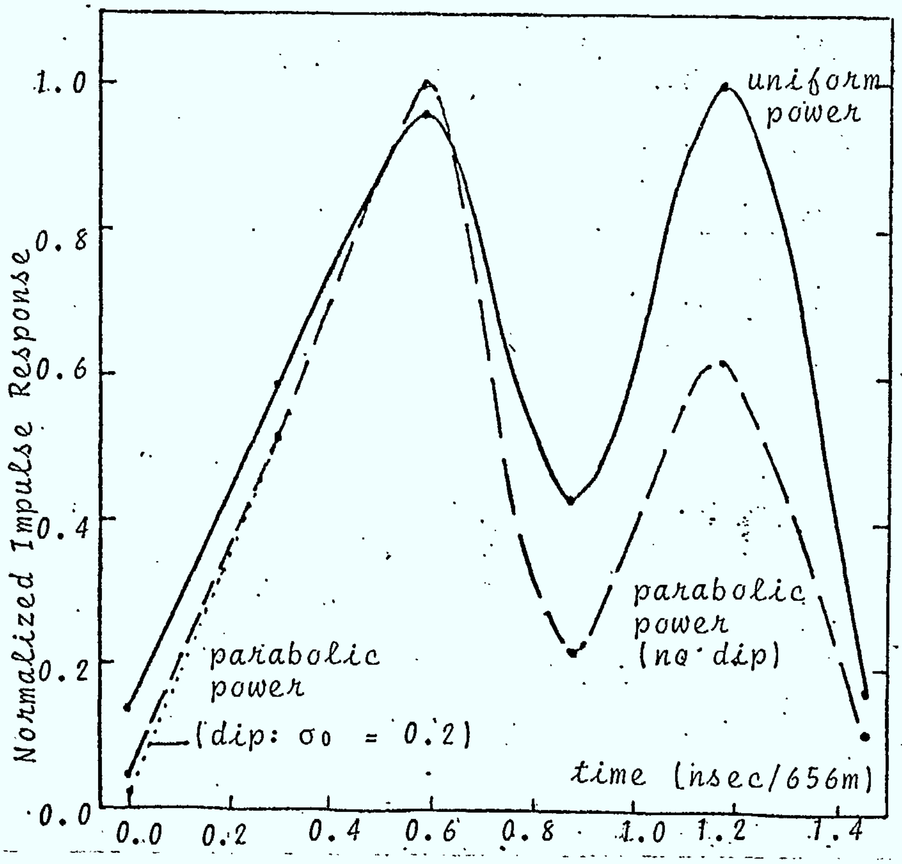

Figure 5.10

Impulse Response of the Test Fiber Computed From the Differential Mode Attenuation, Delay and Excitation of Figs 5.7, 5.8 and 5.9

The FWRMS and FWHM of these impulse responses are 20 to 25% smaller than those of the measured response. The maximum pulse widths are also narrower than the measured one.

The pulse shape is multi-peaked as in the computation based on the measured profile with simulated launching conditions.

The present method is an approximation which implies a one-to-one correspondence between mode (or mode number) and radial position. This assumption is frequently made or implied in the literature. However, most skew rays are omitted from the differential measurements. On the other hand, the finite size and NA of the launch single-mode fiber are such that a few mode groups are excited simultaneously.

Table 5.3 presents in summary form the various pulse broadening results obtained.

Method	FWRMS (nsec/656m)	FWHM (nsec/656m)
Measured Time-Domain	1.04	1.16
Numerical WKB/Profile (SS,NA)		
100%	1.60	1.87
90%	1.57	1.97
80%	1.49	1.95
Numerical DMA, DMD Uniform	0.77	1.10
Parabolic	0.72	0.96
+ DIP	0.73	1.01

Table 5.3 Comparison of the Pulse Broadening of the Test Fiber Obtained from Experimental Time Domain Measurements and from Numerical Simulations via the WKB Model and the Differential Mode Characteristics.

5.2 SOURCE

Modelling the source consists essentially in modelling the modal power distribution (MPD) launched into the fiber. This was done in Section 5.1 to compute the impulse response using either a simulated spot size and launch NA or an input power excitation that is radially uniform or parabolic with or without a central dip.

A better source model was sought, in particular because the WKB model reveals that, for actual fibers, modes with the same propagation constant have different transit times. A relationship between the MPD and the near-field pattern (NFP) was considered using either a geometric optic approach or a field theory approach.

5.2.1 MPD vs NFP: A Geometric Optic Approach

The NFP is viewed as the sum of the contribution of all modes that exist at a given point on the fiber end face. The mode structure is determined by the WKB model. The NFP is taken as

$$N(r)= \sum_{m} r^{-1} w(m,r)\ P(m)\ \cos\Theta(m,r) \tag{5.2}$$

where m represents a mode characterized by its (μ,ν) parameters, where $\Theta(m,r)$ is determined from

$$g(r)+NA^{-2}\sin^{2}\Theta(m,r)= (1-\beta_{\nu\mu}^{2}/n_{o}^{2}k^{2})/2\Delta, \tag{5.3}$$

where the sum extends over all m (or (μ,ν)) such that

$$1-\beta_{\mu\nu}^{2}/n_{o}^{2}k^{2}\geqslant 2\Delta g(r) \tag{5.4}$$

and where $w(m,r)= 2$ if Eqn. (5.3) is satisfied and if $0<\nu=(Vr/a)\sin\Theta(m,r)|\sin\phi|$ is satisfied with $|\sin\phi|\leqslant 1$

$= 1$ if Eqn. (5.3) is satisfied and $\nu=0$

$= 0$ otherwise

P(m) is thought to represent the power carried by a ray of mode (μ,ν). That power is constant along a ray.

Eqn. (5.3) counts all the rays that are congruent to mode (μ,ν), (i.e. they can be made to coincide by an axial displacement or an angular rotation about the fiber axis).

The factor r^{-1} in Eqn. (5.2) has been found to yield nearly satisfactory results but remain otherwise unjustified. Geometric optics predicts that with a lambertian source (i.e. uniform radiance) a NFP proportional to the index profile is obtained when the fiber has neither differential attenuation nor crosscoupling. Figure 5.11 shows the index profile of a fiber and the NFP computed from Eqn. (5.2) when all rays are assumed to carry the same power.

Figure 5.12 shows the same information for an hypothetical linear profile. In both cases the general features and trends of the profile are apparent. The agreement is not as good near the fiber axis where the large 1/r coefficient amplifies any inaccuracy of the method or the model.

When the modal structure of the fiber is known (from the WKB model) the linear transformation of Eqn. (5.2) can in principle be inverted to determine the MPD from a knowledge of the NFP. When the index profile was used as NFP, the resulting MPD was far from uniform and also negative valued. This result is still unexplained.

5.2.2 MPD vs NFP: A Field Theory Approach

Another approach based on field theory was experimented with in an attempt to determine the MPD of a fiber from its NFP. Now the NFP is viewed as the superposition of the power contributed by all modes whose radial field expressions come from Eqn. (3.1.4):

$$NF(r) = \sum_m |E(r,m)|^2 \, w(m)P(m) \qquad (5.5)$$

where $E(r,m)= \dfrac{2}{|rq|^{\frac{1}{2}}} \cos \left(\int_{R_1}^{r} q(r)dr-0.25\pi\right)$ if $R_1<r<R_2$

and

$$E(r,m)= \frac{1}{|rq|^{\frac{1}{2}}} \exp \left(\int_{r}^{R_1} |q(r)|dr\right) \quad \text{if } r<R_1$$

$$E(r,m)= \frac{1}{|rq|^{\frac{1}{2}}} \exp \left(\int_{R_2}^{r} |q(r)|dr\right) \quad \text{if } R_2<r$$

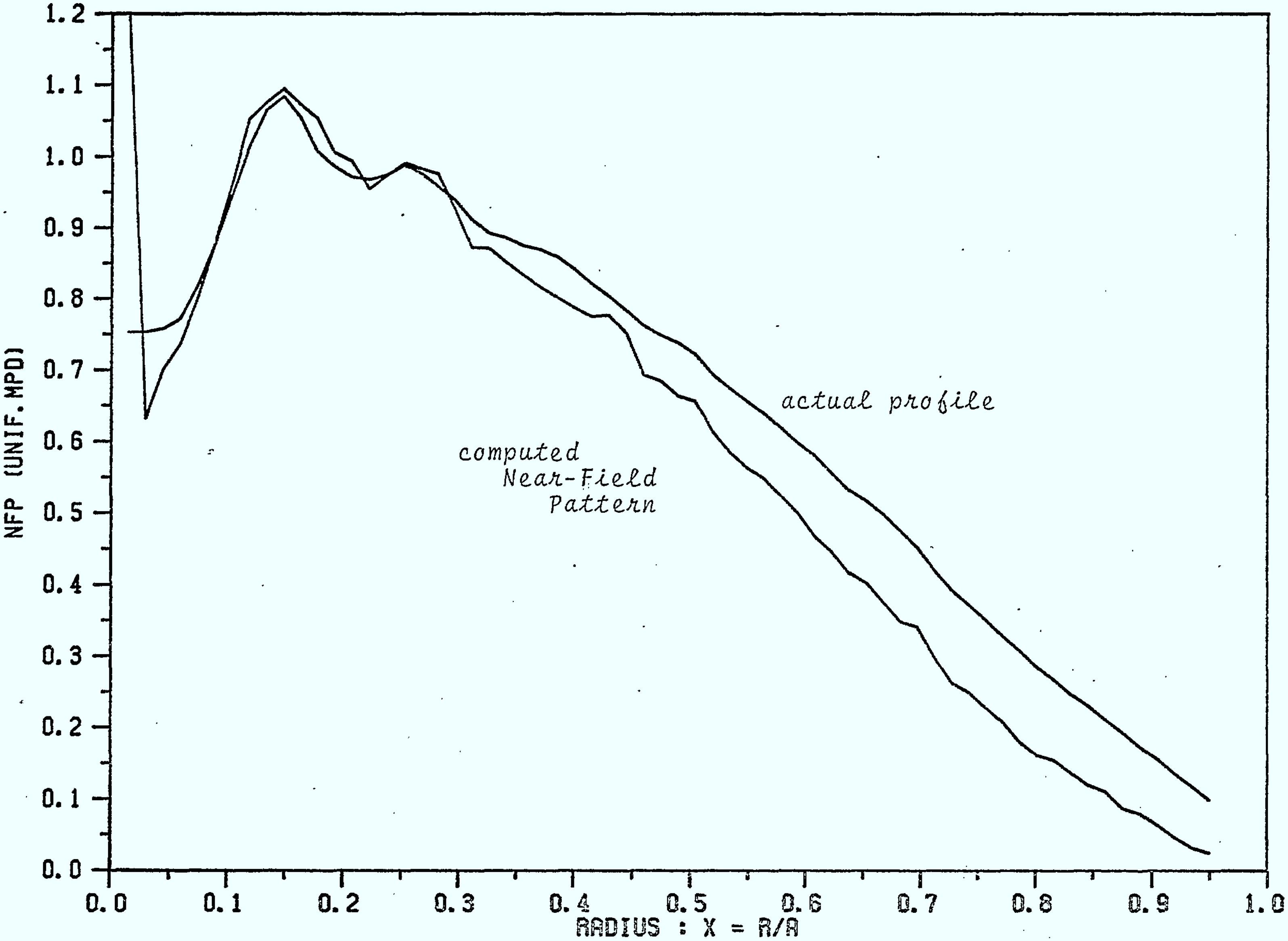

Figure 5.11 Index Profile of an Actual Fiber and the Computed Near-Field Assuming Uniform Power Excitation

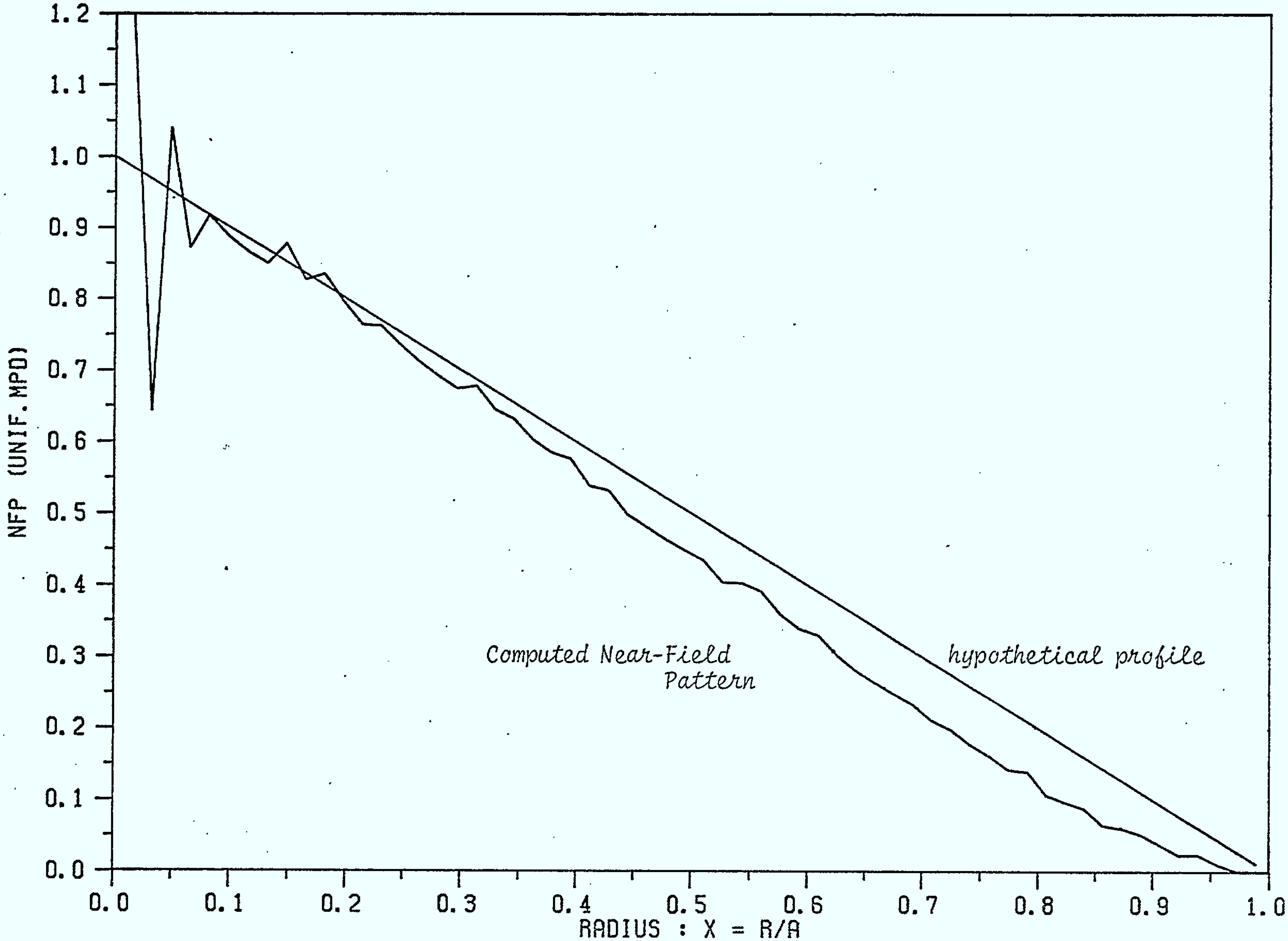

Figure 5.12 Index Profile of an Hypothetical Fiber (Linear Profile: α = 1) and the Computed Near-Field Pattern Assuming Uniform Power Excitation

$$w(m) = 2 \quad \text{if} \quad \nu \neq 0$$
$$\quad\;\; = 1 \quad \text{if} \quad \nu = 0$$

Eqn. (5.5) can also be inverted to yield, in principle, the MPD from the NFP information. The use of the index profile as NFP did result in a MPD that is also negative valued. It is believed this is due to the fact that the WKB method does not describe accurately the modal field in the vicinity of the caustics. Steps will be taken to improve the accuracy of the field expression in the caustics regions.

5.2.3 Significance of the Relationship Between MPD and NFP

The determination of the MPD using the NFP as input would greatly assist the completion of this contract. Thus, a solution to the problems highlighted in the previous sections is actively sought. Once the relationship between MPD and NFP has been established it would be possible to experimentally verify the component models easily. All that would be required are NFP measurements. From NFP measurements taken at the output of a long and a short cut-back fiber length it would be posssible to determine the differential mode delay and attenuation (DMD) and (DMA).

This is in contrast to the situation that will exist if no solution is found. Many complex DMA and DMD measurements will be required to provide experimental verification of the component models.

6. FUTURE ACTIVITIES

The completion of the theoretical analysis will be attempted by focussing on solving the essential problem of determining the modal power distribution. If our current research is successful a relatively simple method of characterizing the MPD will have been found.

The fiber model will be enhanced to include cross-coupling and skew rays.

The joint model will be completed with the inclusion of the power transferred at the joint between the modes for which matching conditions have been established.

The analysis and evaluation of promising launch conditioning devices will commence. The evaluation of the devices will focus on their ability to meet various objective criteria for attenuation and bandwidth test methods.

As a result of both the theoretical and experimental studies, recommendations will be made on suitable techniques to measure the attenuation and bandwidth of fiber links.